Strål
säkerhets
myndigheten
Swedish Radiation Safety Authority

Authors: Jeoung Seok Yoon
Ove Stephansson
Ki-Bok Min

Technical Note

2014:59

Relation between earthquake magnitude, fracture length and fracture shear displacement in the KBS-3 repository at Forsmark

Main Review Phase

Report number: 2014:59 **ISSN:** 2000-0456
Available at www.stralsakerhetsmyndigheten.se

SSM perspektiv

Bakgrund

Strålsäkerhetsmyndigheten (SSM) granskar Svensk Kärnbränslehantering AB:s (SKB) ansökningar enligt lagen (1984:3) om kärnteknisk verksamhet om uppförande, innehav och drift av ett slutförvar för använt kärnbränsle och även inkapslingsanläggning. Som en del i granskningen ger SSM konsulter uppdrag för att inhämta information och göra expertbedömningar i avgränsade frågor. I SSM:s Technical Note-serie rapporteras resultaten från dessa konsultuppdrag.

Projektets syfte

Det övergripande syftet med projektet är att ta fram synpunkter på SKB:s säkerhetsanalys SR-Site för den långsiktiga strålsäkerheten för det planerade slutförvaret i Forsmark. Uppdraget omfattar verifiering av de samband som SKB har tagit fram för att koppla ihop jordskalvmagnituden, spricklängder samt sprickornas skjuvrörelser i KBS-3-förvaret i Forsmark. Oberoende numerisk modellering har genomförts för att verifiera SKB:s resultat men även för att undersöka fall som författarna har bedömt vara signifikanta för granskningen av SR-Site.

Författarnas sammanfattning

Denna studie berör ett av scenarierna som kan försämra den fysiska integriteten av kapslarna i kärnbränsleförvaret i Forsmark. Två källor till skada är: i) termiska skalv pga. värmeutvecklingen från kapslarna som innehåller det använda kärnbränslet, och ii) jordskalv som äger rum vid närliggande deformationszoner och deras möjlighet att initiera sprickbildning hos berget i slutförvaret.

Villkoret som är relevant för förvarets säkerhet gäller skjuvrörelsen på sprickor i berg som induceras antingen av den termiska belastningen, ett närliggande jordskalv, eller av en kombination av dessa två betingelser. I SKB:s säkerhetsanalys SR-Site, antas en skjuvrörelse på 50 mm på sprickor i berg som träffar en kapselposition vara den övre gränsen för kapselbrott. Modellering av termisk belastning samt jordskalv har i denna studie genomförts med PFC2D, en 2-D diskret elementkod. PFC2D-modellerna innefattar ett stort antal explicita deformationszoner, sekundära sprickor samt kapselpositioner, som också fungerar som punktvärmekällor. Horisontella samt vertikala tvärsnittsmodeller av berget i Forsmark har använts i denna studie.

Simulering av jordskalv som sker på en viss deformationszon görs med en plötslig frigörelse av töjningsenergi som byggts upp under rådande bergspänningar och som lagrats i mindre sprickor som bildar deformationszonen i modellen.

Deformationszonerna som finns i modellen har en längd uppmätt vid ytan på mer än 1 km och motsvarar de zoner som har observerats och dokumenterats med hög tilltro av SKB i Forsmark. Nätverk av sekundära sprickor (DFN) med längder mellan 100 och 600 m genereras från sprick-

fördelningar som SKB har tagit fram baserat på sprickkarteringar på plats. Till skillnad mot SKB:s modelleringsstudier har sprickor av olika längd och riktning samt skärningar mellan sprickor explicit modellerats här.

Simuleringarna i denna studie har gett följande resultat: 1) sambanden mellan skjuvrörelser i sekundära sprickor, deras längd och avstånd från skalvets hypocentrum, och 2) seismiska samt icke-seismiska magnituder för termiska, tektoniska, glaciala samt termo-tektoniska inducerade skalv.

Från modelleringen av den värmeinducerade belastningen från det utbrända kärnbränslet visar resultaten att bergmassan expanderar och orsakar skjuvrörelser hos bergsprickor i själva slutförvaret och hos deformationszoner i och omkring slutförvaret. Skjuvningen hos deformationszoner samt sprickor inom varje deponeringsområde i slutförvaret är uppemot 12 mm och minskar i ytterområdena av slutförvaret. För båda fallen där alla bränslekapslar deponeras samtidigt respektive i sekvens, visar resultaten att efter 50 års deponering kommer ingen spricka i slutförvaret att överskrida kriteriet för kapselbrott på 50 mm. Den största magnituden hos jordskalv till följd av den värmeinducerade seismiciteten är M=2,3 och magnituden och frekvensen hos skalven ökar med antalet deponerade kapslar i varje panel i slutförvaret.

Från modelleringen av jordskalv hos horisontella tvärsnittsmodeller genom slutförvaret under nu gällande spänningstillstånd i bergmassan på förvarsdjup, visar resultaten att ett jordskalv med magnitud M~5 hos deformationszonen ZFMWNW0809A kan generera ett medelstort inducerat skalv hos deformationszonen ZFMNW1200 som befinner sig på relativt stort avstånd från zonen ZFMWNW0809A. Simulering av ett jordskalv i deformationszonen ZFMWNW2225 resulterar i ett skalv på M~4 samt att ett mindre antal sekundära sprickor i slutförvaret kan komma att skjuvas mera än 50 mm. Singöförkastningen ZFMWNW0001 representeras i modellerna av en förkortad deformationszon. Aktiveringen av ett jordskalv i zonen simuleras genom att tvinga skjuvkrafterna längs zonen till en storlek som resulterar i ett skalv med magnituden M~6 eller högre, vilket leder till skjuvning hos bergsprickor i slutförvaret som överstiger gränsen för kapselbrott.

Modellering av jordskalv har också utförts för ett antal deformationszoner under glaciala spänningstillstånd hos berget i Forsmark. Resultaten visar något högre skalvmagnituder än för fallet med modellering med dagens antagna spänningstillstånd hos bergmassan. Simulering av jordskalv för ytterligare två av deformationszonerna, ZFMWNW0001 samt ZFMWNW2225, resulterar i en skjuvrörelse hos sprickor i slutförvaret som överstiger gränsvärdet på 50 mm.

Jordskalv har också simulerats i vertikala tvärsnittsmodeller genom slutförvaret där en grupp av flacka deformationszoner (ZFMA2, ZFMA3, ZFMA8 och F1) aktiverades vid samma tidpunkt. Resultaten visar att gränsvärdet på 50 mm överskrids hos sprickor i slutförvaret under de båda antagandena att dagens tektoniska spänningar verkar i berget och att området täcks av en inlandsis i samband med glaciationsmaximum.

Resultaten från modellering av slutförvarets respons på en samtidig termal belastning och jordskalv visar att skjuvning av bergsprickor och deformationszoner som inducerats genom termisk belastning förstärks med en faktor 3 genom inverkan av jordskalvet. Skalvmagnituden under termisk belastning ökar också för de seismiska skalven samt för de inducerade skalv jämfört med fallet utan termisk belastning. Simuleringsresultaten visar också att jordskalv som initieras på deformationszonerna ZFMWNW0809A och ZFMWNW2225 cirka 50 år efter att en sekventiell deponering startat och temperaturen i närområdet nått sitt maximum, leder till skjuvning av bergsprickor som överskrider gränsvärdet på 50 mm för kapselbrott.

Av resultaten från utförda modelleringar i denna studie drar författarna slutsatsen att risken för att kapselbrott kan ske, utöver vid stora glaciala skalv, för det fall att ett större jordskalv inträffar i någon av de omkringliggande stora deformationszonerna vid tiden för drift av slutförvaret och under den termiska fasen.

Projektinformation
Kontaktperson på SSM: Flavio Lanaro
Diarienummer ramavtal: SSM2011-3631
Diarienummer avrop: SSM2013-3839
Aktivitetsnummer: 3030012-4077

SSM perspective

Background

The Swedish Radiation Safety Authority (SSM) reviews the Swedish Nuclear Fuel Company's (SKB) applications under the Act on Nuclear Activities (SFS 1984:3) for the construction and operation of a repository for spent nuclear fuel and for an encapsulation facility. As part of the review, SSM commissions consultants to carry out work in order to obtain information and provide expert opinion on specific issues. The results from the consultants' tasks are reported in SSM's Technical Note series.

Objectives of the project

The general objective of the project is to provide review comments on SKB's post-closure safety analysis, SR-Site, for the proposed repository at Forsmark. In particular, this assignment concerns the verification of the relations obtained by SKB for linking earthquake magnitude, length of the fractures, shear displacement on the fractures in the KBS-3 repository at Forsmark. Independent numerical earthquake modelling is carried out for verifying some of SKB's results but also for covering cases the Authors judge are necessary for the assessment of SR-Site.

Summary by the Authors

This study addresses one of several scenarios that could impair the physical integrity of the repository of spent nuclear fuel at the Forsmark site. Two sources of threat are: i) events due to thermal loading on the rock mass by the heat from canisters with spent nuclear fuel, and ii) seismic events, i.e. earthquakes, at the nearby deformation zones and zones intersecting the repository area.

The effect relevant to the repository safety is the shear displacement on rock fractures induced either by the effect of thermal loading, or by an earthquake at a nearby deformation zone, or by the combination of the two. In SKB's safety assessment SR-Site, a shear displacement of 50 mm of a target fracture that crosses a canister position in the repository area is regarded as the upper limit of canister failure.

Thermal loading and earthquake simulations in this study are conducted using PFC2D, a 2-D discrete element code. The PFC2D models include a large number of explicitly modelled deformation zones, target fractures and canister positions, which acts as point-heat sources. Horizontal and vertical cross-sections of the site are considered in this study.

Earthquake at a specific deformation zone is simulated by a sudden release of the strain energy that was accumulated under the given in situ stress condition and stored in smaller fractures building up the deformation zones.

The deformation zones included in the model have a surface length greater than 1 km and were observed and documented with high confidence of existence at the Forsmark site by SKB. Networks of target fractures

(DFN) with length between 100 m and 600 m are generated from distributions built by SKB based on observations at the site. Unlike SKB's studies of earthquakes, the target fractures in the models in this study have various lengths and orientations, and can intersect one another.

The main outputs from the simulations in this study are: 1) shear displacement of the target fractures with respect to the fracture length, and 2) seismic and co-seismic magnitudes of the thermally, earthquake, glacial-earthquake and thermal-and-earthquake induced events.

From the modelling of heat induced repository responses, it is observed that the repository rock mass expands due to the heat and induces shear displacement of the target fractures and the nearby deformation zones. Shear displacements are up to 12 mm for those fractures located within the footprint of the heated panels, and relatively smaller at the outskirts of the heated panels. In both cases where the canisters are disposed simultaneously and sequentially, the results show that the fractures do not slip more than the canister damage threshold within the 50 years after start of deposition. The heat induced seismicity tends to increase with the number of canisters disposed in the panels, and the largest magnitude is M=2.3.

From the modelling of the repository responses to seismic events under present-day stress condition at Forsmark, it is found that an earthquake at zone ZFMWNW0809A might have a magnitude of M~5 and can trigger moderately large magnitude co-seismic events at zone ZFMNW1200, which locates at a far distance from zone ZFMWNW0809A. An earthquake simulation is done to the zone ZFMWNW2225 that intersects the repository panels. An active earthquake on this zone results in M~4 and shows that some of the target fractures can shear more than 50 mm. The major Singö fault zone ZFMWNW0001 is represented by a truncated trace in the model. Modelling of an earthquake is simulated by forcing the shear force along its trace and yields to a magnitude M~6 or larger, and shows that some of the target fractures can shear more than 50 mm. Earthquake modelling is done at a few selected deformation zones under the glacial stress conditions (forebulge and maximum thickness of ice cover for the horizontal model, and maximum ice cover and ice retreat for the vertical model). The results show that the magnitudes tend to be higher than those for the present-day stress condition, which is attributed to more anisotropic and higher stresses caused by the ice cover. Modelling of earthquakes at two zones, ZFMWNW0001 and ZFMWNW2225 with M~6 and M~4, respectively, pose risks that some of the target fractures can shear more than 50 mm.

Earthquake modelling is done with the vertical section models where a group of closely spaced and gently dipping zones (ZFMA2, ZFMA3, ZFMA8 and F1) are activated at the same time. The resulting magnitudes are above M=5.5 and results show that some of the target fractures can shear more than 50 mm under the stress conditions at present day and at the time of maximum ice cover.

From the modelling of thermal-and-earthquake induced repository responses, it is found that the shear displacements of target fractures and deformation zones induced by the heating are powered by the effect of the earthquake up to a factor 3. Also the intensity of the seismic events that strikes during heating is magnified by the heating. Both modelling cases where an earthquake takes place at zone ZFMWNW0809A and ZFMWNW2225 at 50 years after the start of sequential deposition show that some of the target fractures can give shear displacements larger than 50 mm.

From the results of the modelling cases conducted in this study, the Authors draw the conclusion that there might be a risk for canister damage, other than for the conditions with glacially induced earthquakes, also for the conditions when an earthquake at a nearby deformation zone hits the repository during the operational and thermal phases.

Project information
Contact person at SSM: Flavio Lanaro

Strål
säkerhets
myndigheten
Swedish Radiation Safety Authority

Authors: Jeoung Seok Yoon[1], Ove Stephansson[1] and Ki-Bok Min[2]
[1] Stephansson Rock Consultant, Berlin, Germany
[2] Seoul National University, Seoul, South Korea

Technical Note 74; page -60

2014:59

Relation between earthquake magnitude, fracture length and fracture shear displacement in the KBS-3 repository at Forsmark

Main Review Phase

Date: December 2014
Report number: 2014:59 **ISSN:** 2000-0456
Available at www.stralsakerhetsmyndigheten.se

This report was commissioned by the Swedish Radiation Safety Authority (SSM). The conclusions and viewpoints presented in the report are those of the author(s) and do not necessarily coincide with those of SSM.

Contents

1. Introduction

This assignment is a part of Main Review Phase conducted by the Swedish Radiation Safety Authority (SSM) on the SR-Site safety assessment of the final disposal of spent nuclear fuel at Forsmark in the application for construction license submitted by the Swedish Nuclear Fuel and Waste Management Company (SKB).

This assignment concerns an assessment of the relation between earthquake magnitude, length of a rock fracture and its response to shear displacement. SKB's account assumes a certain relation between the earthquake magnitude and the amount of shear displacement that rock fractures (i.e. target fractures) can experience at a distance from the hypocentre. This means that the amount of shear displacement would diminish for target fractures away from the hypocenter. Due to uncertainties on the deformation zone model, on the frequency and magnitude of possible earthquakes, on the occurrence and position of target fractures and their reciprocal interaction during an earthquake at Forsmark, it can be assumed that the shear displacements that could possibly occur on a certain fracture must be represented by a frequency distribution of displacements. This is done by SKB by assuming a constant frequency distribution between a zero displacement and a maximum displacement value (Fälth et al. 2010).

1.1. Background

SKB has conducted numerical modelling studies where earthquakes are simulated in a generic way with the distinct element code 3DEC, and investigated responses of the target fractures (Fälth et al., 2010). They concluded that the 3DEC models produce peak ground accelerations and velocities that are in accordance with those from records of real earthquakes. They also argued that the models used and the modelling technique adopted (mesh, boundary conditions, treatment of rupture initiation and propagation) are adequate for the intended license application.

However, SKB's modelling has some idealizations and the method used seems to have some major limitations. The Authors consider that SKB's results may be limited in scope and the method might not be appropriate for solving this type of problems, in particular when dealing with geological structures with high complexity such as in Forsmark. Therefore, the Authors list below a few major limitations of the method and modelling approach that SKB has adopted:

- Only one primary fault is considered in each model and is represented by a planar feature inside a large rock block, which is assumed to be a linear elastic, isotropic, homogeneous and continuous medium.
- The vertical stress corresponds to the rock overburden in all models while the horizontal stresses are calibrated to produce the intended seismic moment, given the prescribed rupture area and the properties of the surrounding rock mass.
- Attenuation of seismic wave is not accounted for.
- All modelled target fractures are planar, have uniform properties over their entire surface area and have uniform in size, i.e. a radius of 150 m.
- All modelled target fractures have strike parallel to the primary fault.

- All modelled target fractures are isolated and interactions through intersections are not taken into account, which may have drastic impacts on the shear displacements.
- Normal stiffness and shear stiffness of the target fractures are generic.
- Dilation is not assumed in the modelled target fractures.
- The deformation zone friction angle and cohesion are fictitious, with no coupling to real site data.

From the issues mentioned above, the Authors argue that the modelling conducted by SKB, although it is in 3D, bears some idealization of the material properties and geometries of key geological structures.

Therefore, in the modelling study in this assignment, the Authors try to overcome these limitations by making the model resemble the geological structures at Forsmark site as close as possible.

1.2. Assigned topics

This study produces independent verification analyses to SKB's presentations and tackles the technical issues that were not covered in sufficient detail by SKB for the construction licence application of the final repository for spent nuclear fuel at Forsmark. The following tasks are performed in this study:

- Task A: Review of the earthquake modelling studies conducted by SKB,
- Task B: Presentation of the modelling method with Particle Flow Code (PFC) used in this study,
- Task C: Generation of a discrete element model for Forsmark with deformation zones and discrete fracture networks,
- Task D: Modelling of a generic earthquake with PFC,
- Task E: Analysis of target fracture and of the repository responses due to heating from the spent nuclear fuel,
- Task F: Analysis of target fracture and of the repository responses due to tectonic and post-glacial earthquake at nearby major deformation zones,
- Task G: Analysis of target fracture and of the repository responses due to a combination of heating from the spent nuclear fuel and earthquake.

Task A undertakes a literature review of the existing knowledge about thermal induced and earthquake induced shear behaviour of fractures in a repository conducted by SKB. This is covered in Chapter 2.

Task B presents a literature review of the PFC modelling method used in this study. The main focus is to demonstrate that PFC as a modelling method is a suitable choice for this assignment. This is covered in Chapter 3.

Task C focuses on describing the procedure for model generation, where SKB's local model area of Forsmark site is transformed into horizontal and vertical section models based on the discrete element method with realistic representation of deformation zones and discrete fracture network. This is covered in Chapter 4, Sec. 4.1 through 4.7.

Task D focuses on describing the procedure for simulation of a generic earthquake at a major deformation zone in the discrete element model. This is covered in Chapter 4, Sec. 4.8 through 4.10.

Task E undertakes analysis of target fracture responses due to thermal loading induced by the heat from the spent nuclear fuel. This is covered in Chapter 5.

Task F undertakes analysis of target fracture responses due to seismic loading induced by tectonic and post-glacial earthquakes at nearby major deformation zones. This is covered in Chapter 6.

Task G undertakes analysis of target fracture responses due to the combination of thermal and seismic loading induced by tectonic earthquakes at major deformation zones. This is covered in Chapter 7.

Appendix 1 lists the main SKB references reviewed in this report.

Appendix 2 reports the quality checks for the DFN models used in this report.

As quite a number of modelling cases are investigated, there are many similar plots. Instead of presenting all figures in the body text, only the key plots are reported and discussed here. All the rest of the result plots are presented in Appendix 3.

2. Review of the studies conducted by SKB

2.1. SKB's analysis of thermal induced target fracture responses

Modelling of post-glacial earthquake by Fälth et al. (2010) was done without consideration of the actual stress situation or the actual geometry of the deformation zones at Forsmark. Such a schematic calculation approach does not work for analysis of thermally induced earthquake since the exact position of repository with respect to the geological features is crucial for the thermo-mechanical loading and potential earthquakes on deformation zone.

Therefore, a recent modelling study by Fälth and Hökmark (2013) considers specifically designed, site-specific thermal loading models with corresponding site-specific post-glacial loading conditions. This investigates heat induced shear displacement of target fractures. The main conclusion is that the effects of thermally induced earthquakes are sufficiently smaller than those due to post-glacial fault movements when the ice retreats during future glaciations.

Following are the major conclusions from SKB's study.

- The average displacement due to an earthquake on the thermally affected deformation zone ZFMA2 is about 60% of the average displacement due to post-glacial displacement for an earthquake of the same magnitude.
- The thermal disturbance of the stability of the deformation zone ZFMA2 is negligible.
- Due to the conservative assumption about the strength of zone ZFMA2, the magnitude of the earthquake assumed for the zone ZFMA2 is M5.5 at the highest.
- The difference between the maximum induced shear displacement of target fractures due to an earthquake that occurs after 100 or 1000 years of heating is negligible.
- The maximum secondary shear displacement of the heated target fractures at the foot wall side of the zone is 80% of the post-glacial case. A target fracture with radius of 150 m at 200 m distance from zone ZFMA2 gives a induced shear displacement during heating of 19 mm, which is around 40% of the maximum displacement allowed of 50 mm.
- SKB claims that there is little risk of canister damage due to fracture shear caused by an earthquake occurring during the thermal phase, and the large displacement calculated for zone ZFMA2 is not likely.

2.2. SKB's analysis of earthquake induced responses of target fracture

Given the bounding assumptions of planar fracture geometry, uniform properties and elastic continuum medium discussed briefly in Sec. 1.1, Fälth et al. (2010) have

made the following observations regarding the response of the target fractures to an earthquake:

- There is a strong correlation between the amount of induced target fracture shear displacement and the distance from the fault.
- The shear displacement decreases with distance in approximately the same way regardless of the slip mechanism, i.e. whether fractures slip because of a temporary loss of strength or because of stress redistribution.
- The shear displacement of target fracture scales linearly with the size of the fracture. This should be expected for a fracture in an infinite elastic medium with one embedded fracture subjected to quasi-static loading, but is assumed to hold true also for the type of dynamic impact generated by slipping earthquake faults.

2.3. SKB's analysis of post-glacial earthquake induced responses of target fracture

Modelling of post-glacial earthquakes by Fälth et al. (2010) was done without consideration of actual stress situation or the actual geometry of deformation zones at Forsmark. Recent modelling studies by Fälth and Hökmark (2013) consider the actual geometry of deformation zones and site-specific post-glacial loading conditions. In this later study, they also looked into the issue whether an earthquake occurrence at zone ZFMA2 can have effects on the intersecting the zone ZFMNW0017. Following are brief conclusions drawn from their study:

- The influence of the interaction between deformation zones on the secondary induced fracture displacement is found to be small.
- Compared to the databases and regressions by Wells and Coppersmith (1994), and Leonard (2010), the synthetic site-specific earthquake on zone ZFMA2 assumed in Fälth et al. (2013) produces a shear displacement of 1.8 m and a magnitude of Mw5.6 that are larger than in Fälth et al. (2010).
- Target fractures in the model are in principle isolated. When fractures are connected in the form of a discrete fracture network, displacements will be slightly smaller because the movement of adjacent and intersecting fractures will absorb some of the strain energy.
- On the foot wall side of zone ZFMA2 where deposition areas are located, fracture shear displacement is not greater than 30 mm.

2.4. The Consultants' assessment

Even though the sounding conclusions by SKB listed above, the Authors argue that it is not enough to draw conclusive statements such as that the probability of canister failure due to shear displacement on the target fracture exceeding 50 mm is zero. It is necessary to conduct more detailed analyses to demonstrate that this threshold is not overcome, by using a realistic discrete fracture network and several deformation zones observed and documented by SKB with high confidence of existence at the site. Furthermore, it is not clear if SKB has explicitly considered the effects thermal loading on target fractures and deformation zones due to the heat from the canisters that are disposed in a simultaneous or sequential way, i.e. heat release from panel A to panel D.

Furthermore, assuming the rock mass to be an elastic medium is a rather unrealistic assumption. Although this assumption may give more conservative result in terms of shear displacements on target fractures, it may hold valid only if the investigated geometry is relatively simple, i.e. for a single fault, uniform size of the isolated fractures that are separated by uniform spacing distance, and when propagation is not allowed. This means that complex geometries where embedded large faults and small fractures can intersect one another, elasto-plastic behaviour of the rock matrix where damage is taken into consideration and can lead to coalescence of smaller fractures and results in growth at larger scales, cannot be considered.

3. The Consultants' independent modelling method

This Chapter deals with a review of some key references where Particle Flow Code (PFC) was used to solve Rock Engineering problems. The first part introduces the basic theory of PFC.

3.1. Bonded Particle Model and Particle Flow Code

In this assignment, the Authors use bonded-particle model (BPM) where they argue that rock behaves like a cemented granular material of complex-shaped grains in which both the grains and the cement are deformable and may break. Such a conceptual model can explain many aspects of the physical and mechanical behaviour of rock materials.

In BPM, unlike in Finite Element Method (FEM), rock damage is represented directly by the breakages of individual structural units or bonds. The BPM simulates the mechanical behaviour of a collection of non-uniform-sized circular or spherical rigid particles with geometric density that may be bonded together at their contact points. The rigid particles interact only at the soft contacts, which possess finite normal and shear stiffness. The mechanical behaviour of this system is described by the movement of each particle with respect to each other and the force and moment acting at each contact.

Newton's second law of motion provides the fundamental relation between particle motion and the resultant forces and moments causing that motion, which is shown in Figure 1.

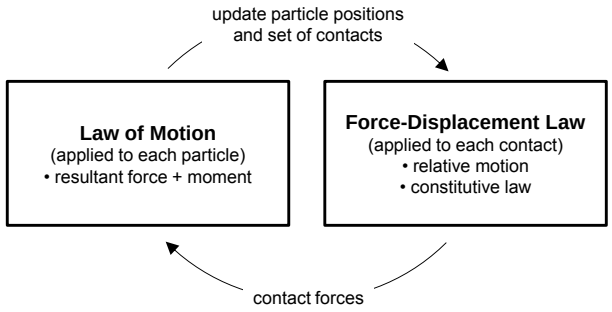

Figure 1. Calculation cycle for BPM in PFC (Itasca, 2009).

The following assumptions are inherent in the BPM:

- The particles are circular or spherical rigid bodies with a finite mass.
- The particles move independently of one another and can both translate and rotate.
- The particles interact only at contacts; because the particles are circular or spherical, a contact is comprised of only two particles.

- The particles are allowed to overlap one another, and all overlaps are small in relation to particle size such that contacts occur over a small region (i.e. at a point).
- Bonds of finite stiffness can exist at contacts, and these bonds carry load and can break.
- Generalized force-displacement laws at each contact relate relative particle motion to force and moment at the contact.

The BPM is implemented in the two and three dimensional discontinuum programs Particle Flow Code (PFC) by Itasca using the Distinct Element Method (DEM). In the DEM, the interaction of the particles is treated as a dynamic process with states of equilibrium developing whenever the internal forces balance. The contact forces and displacements of a stressed assembly of particles are found by tracing the movements of the individual particles. Movements result from the propagation through the particle system of disturbances caused by wall and particle motion, externally applied forces and body forces.

The calculations performed in the DEM alternate between the application of Newton's second law to the particles and a force-displacement law at the contacts (Figure 1). Newton's second law is used to determine the translational and rotational motion of each particle arising from the contact forces, applied forces and body forces acting upon it, while the force-displacement law is used to update the contact forces arising from the relative motion at each contact.

The dynamic behaviour is represented numerically by a time-stepping algorithm in which the velocities and accelerations are assumed to be constant within each time step. The use of an explicit, as opposed to an implicit, numerical scheme provides the following advantages. Large populations of particles require only modest amounts of computer memory, because matrices are not stored. Also, physical instability may be modelled without numerical difficulty, because failure processes occur in a realistic manner; it is not necessary to invoke a non-physical algorithm, as is done in some implicit methods.

In the following sections, key modelling methods and techniques used in this assignment are briefly described and some key papers published by the Authors and several others are listed.

3.2. Fracture propagation modelling

Yoon (2007) and Yoon et al. (2012) have conducted a series of numerical modelling studies using PFC2D and investigated fracture and friction behaviours of crystalline brittle granite deformed under confined asymmetric loading (Zang et al., 2002). From the study, it turned out that the PFC2D modelling can be successfully applied for simulating initiation and propagation of fractures in brittle rock while other modelling methods, e.g. x-FEM, are unable to handle this type of problems (Dumstorff et al., 2006).

The simulated fracture paths with PFC2D match that observed from laboratory experiments on rock core samples under asymmetric compressive tests with various confinements. Under low confinement (< 5 MPa), the fracture initiates in Mode I from the edge of the asymmetric loading platen and propagates toward the unloaded portion of the granite sample (Figure 2a, top). Under higher confining pressure (10 MPa), after nucleus of Mode I fracture, an inclined rupture path develops and propagates towards the loaded portion of the model (Figure 2a, bottom). Modelling studies by Yoon (2007) using conventional particle model incorporated the concept

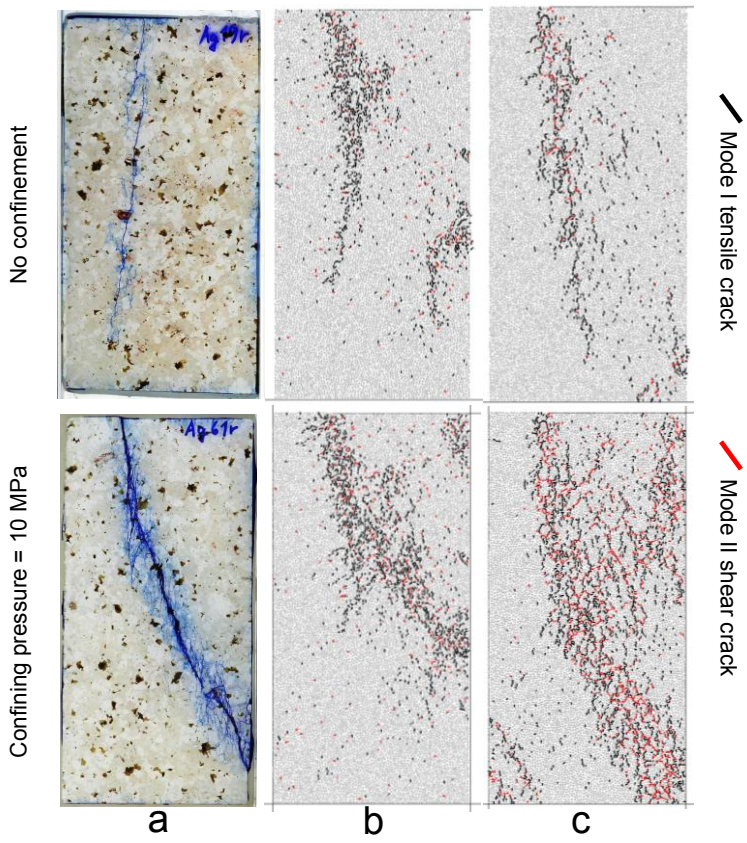

Figure 2. Fracture propagation paths in asymmetric compressive loading from: (a) laboratory observation (Zang et al., 2002), (b) conventional particle modelling (Yoon 2007), (c) clumped particle modelling (Yoon et al., 2012).

of rock fracture toughness in Mode I and II in the model parameterization and calibration and the resulting fracture propagation paths matched closely the laboratory observation (Figure 2b). Modification in the model setup was done using clumped particle model in Yoon et al. (2012) and the results matched better the laboratory observations (Figure 2c).

3.3. Synthetic rock mass modelling

PFC has shown the ability to reproduce features of the initiation and propagation of fracturing in rocks and jointed rock masses (Potyondy & Cundall 2004; Yoon et al., 2012). Kulatilake et al. (2001) demonstrated the use of PFC3D in modelling jointed rock block behaviour under uniaxial loading. Their model geometry was relatively simple, involving a few persistent through-going joints in a lab scale sample. Park et al. (2004) created more densely jointed 2D rock mass models with PFC2D by incorporating up to 100 joints from a discrete fracture network in a 30 m × 30 m block. They also demonstrated that the number of joints has a significant impact on the strain-softening behaviour, changing from brittle to ductile for an increasing number of joints.

The advantage of PFC modelling is that it allows for consideration of block breakage, including the impact of incomplete joints on block strength and deformability. The Synthetic Rock Mass modelling (SRM) method is based on the

generation and testing of 3D numerical synthetic rock mass samples (Figure 3b). This new technique brings together two well-established techniques: the bonded particle model for rock (Figure 3c, left), developed by Potyondy and Cundall (2004) for the simulation of intact rock deformation and brittle fracture, and the discrete fracture network (DFN, Figure 3a) (Derschowitz & Einstein, 1998) for the representation of the rock mass in-situ joint fabric. Each individual joint is represented explicitly within the SRM sample making use of the recently developed smooth-joint contact model (Figure 3c, right). This new technique of joint representation in PFC3D has made it possible to extend the approach of Park et al. (2004) to volumes of rock at the scale of 10 to 100 m containing thousands of non-persistent joints.

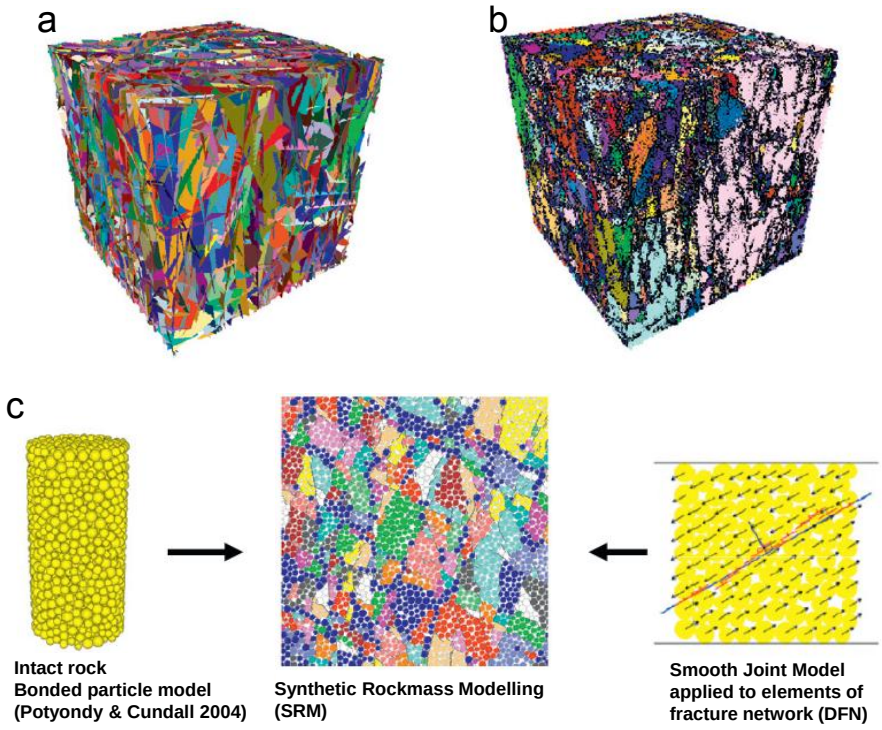

Figure 3. 3D DFN and the corresponding 3D synthetic rock mass model, and basic components of Synthetic Rock Mass (modified from Mas Ivars et al., 2011).

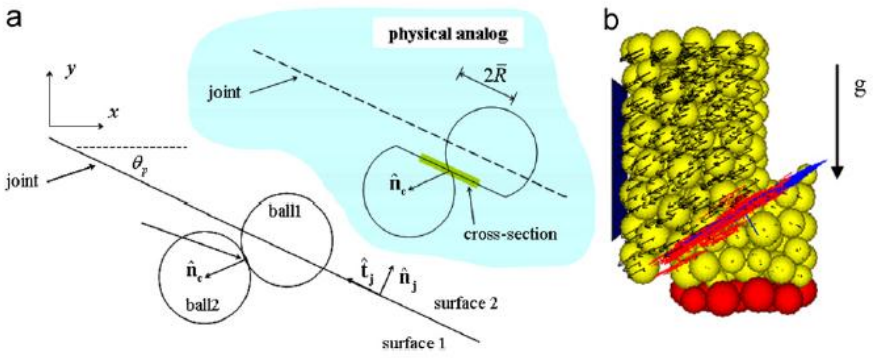

Figure 4. Joint geometry and a 3D specimen with frictional through-going joint loaded by gravity. Large shearing motion results in the creation of new smooth-joint contacts along the joint plane (Mar Ivars et al., 2011).

Intact rock is represented in the SRM samples by the bonded particle model for rock. A more detailed explanation of the BPM for rock can be also found in Potyondy and Cundall (2004). In a BPM, microcracks are able to form, interact, and coalesce into macroscopic fractures according to local conditions. In this manner, macroscopic material behaviours not encompassed by current continuum theories can be investigated. The BPM has a demonstrated ability to reproduce many features of rock behaviour, including elasticity, fracturing (Yoon, 2007; Yoon et al., 2012), acoustic emission (Hazzard & Young, 2002, 2004; Yoon et al., 2012), damage accumulation producing material anisotropy, hysteresis, dilation, post-peak softening, and strength increase with confinement.

Interfaces in numerical models consisting of assemblies of bonded particles have been traditionally represented by de-bonding contacts along a line or a plane and assigning low strength and stiffness micro-properties to them. This way of representing interfaces is problematic because of the inherent roughness of the interface surfaces. Even the assignment of very low friction to the contacts on the interface generally does not lead to realistic sliding because of the roughness or bumpiness induced by the particles. Small particles may be used to represent the interface as a softer and weaker band, with several particles across the band to minimize the roughness. However, this is not feasible when the model requires a large number of interfaces.

To overcome this problem, Cundall proposed the concept of the "smooth-joint contact model" (Mas Ivars et al., 2008). The smooth-joint contact model simulates the behaviour of a smooth interface, regardless of the local particle contact orientations along the interface as shown in Figure 4. More detail of the behaviour of smooth joint contacts can be found in Mas Ivars et al. (2011).

SRM has been applied to the geomechanical characterization of coal seam reservoirs (Deisman et al., 2008, 2010; Esmaieli et al., 2009), the study of the effect sample size on rock mass strength (Esmaieli et al., 2009), and the study of the influence of veining in intact rock strength (Pierce et al., 2009). Zang et al. (2013) and Yoon et al. (2014) also used SRM and smooth joint contact model in the study of fluid injection induced seismicity in naturally fractured reservoirs.

A similar approach, making use of the SRM concept has been used for the stability analysis of vertical excavations in hard rock by Hadjigeorgiou et al. (2009) where smooth joints were used to mimic the in situ joint fabric and applied to a field case study of a mine in northern Quebec. First, fracture system was created (Figure 5a) which is later then linked to PFC3D to create fractured rock mass (Figure 5b). Successful linking of a 3D fracture generator and PFC3D allowed better insight on the interaction of structures and stress. It was possible to consider the structurally defined wedges and to visualize both gravity fall and sliding of unstable wedges.

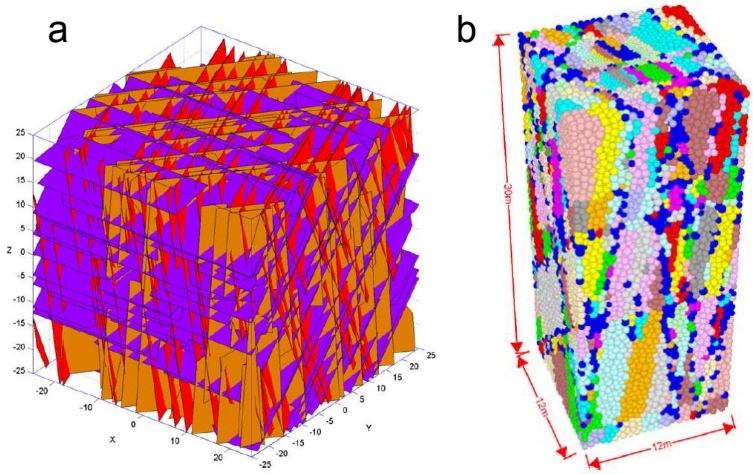

Figure 5. (a) 3D representation of fracture system, (b) generated 3D rock mass model to mimic the in situ joint fabric (Hadjigeorgiou et al., 2009).

3.4. Coupled thermo-mechanical modelling

The thermal option of PFC allows simulation of transient heat conduction and storage in materials consisting of bonded particles, and development of thermally induced displacements and forces. The thermal material is represented as a network of heat reservoirs (associated with each particle) and thermal pipes (associated with the contacts). Heat transfer by radiation and convection are not included in the present formulation. Thermally induced strains are produced in PFC material by modifying the particle radii as a function of heat expansion coefficient and the force carried in each parallel bond to account for heating of both particles and bonding material.

For the detailed explanation of the theory and application, the reader should refer to Wanne and Young (2008) where a numerical modelling study of a heated rock and validation of the modelling results by a laboratory experiment was carried out.

The following four micro-properties are used by the PFC2D thermal logic:

- Density ρ (kg/m^3) of each particle,
- Specific heat at constant volume Cv (J/kg-C),
- Coefficient of linear thermal expansion α (1/C) of each particle,
- Thermal resistance per unit length η (C/W-m) of each pipe.

Thermal strains are produced in the bonded particle model by accounting for the thermal expansion of the particles and of the bonding material that joins them. The thermal expansion is applied by a given temperature change ΔT resulting in a change of particle radius R by

$$\Delta R = \alpha R \Delta T \qquad \text{Eq. (3-1)}$$

where α is the coefficient of linear thermal expansion associated with the particle.

If a parallel bond is present at the contact associated with a pipe, then it accounts for the expansion of the bond material by assuming that only the normal component of the force vector carried by the bond ΔF^n will be affected by the temperature change. An isotropic expansion of the bond material, effectively changes the bond length, L, taken equal to the distance between the centroids of the two particles at the ends of

the pipe associated with the bond. This is modelled by changing the normal component of the bond force vector as:

$$\Delta F^n = -k^n A \Delta U^n = -k^n A(\alpha L \Delta T) \qquad \text{Eq. (3-2)}$$

where k^n is the bond normal stiffness, A is the area of the bond cross section, α is the expansion coefficient of the bond material (taken equal to the average value of the expansion coefficients of the particles at the two ends of the pipe associated with the bond), and ΔT is the temperature increment (taken equal to the average temperature change of the two particles at the ends of the pipe associated with the bond).

Wanne and Young (2008) conducted PFC2D modelling where thermo-mechanical coupling is taken into account. The numerical results were compared directly to the corresponding laboratory experiment (Figure 6a) where a heated cartridge was placed into a central borehole in a cylinder of Lac du Bonnet granite in order to see and monitor by acoustic emission how the fracture initiates at one of the perimeters and propagates. It was concluded that the locations of the micro-cracking during pre- and post-failure in the model (Figure 6b) and in the experiment (Figure 6c) are qualitatively matching. The model captured the behaviour of the laboratory experiment relating to the macroscopic tensile failure driven by high hoop stresses. This study has demonstrated that capability and reliability of the coupled thermo-mechanical modelling in PFC2D is verified.

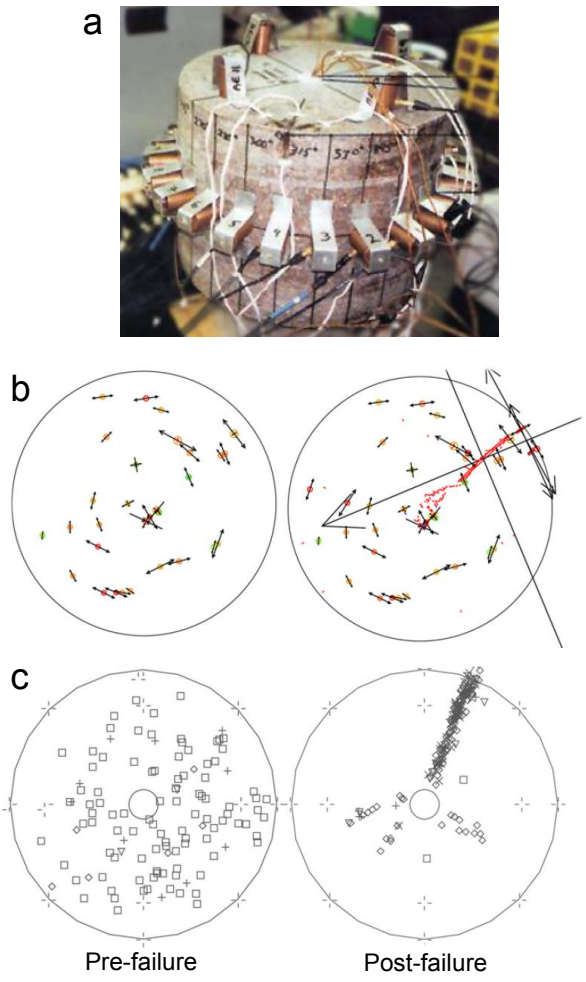

Figure 6. (a) Lac du Bonnect granite specimen tested with AE sensors, (b) pre- and post-failure crack events simulated by PFC2D, (c) pre- and post-failure AE events monitored in the experiment (Wanne & Young, 2008).

3.5. Seismicity modelling

Each bond breakage in the bonded particle assembly is assumed to represent a fracturing process associated with seismic energy radiation. PFC runs in dynamic mode with low levels of numerical damping where a realistic level of energy attenuation in the rock is simulated. Upon a bond breakage in Mode I or Mode II, part of accumulated strain energy at the broken bond is released to the surroundings in the form of seismic wave. A numerical technique for calculating the seismic source information in PFC2D has been proposed by Hazzard and Young (2002 and 2004).

Modification was made to the algorithm to compute seismic source parameters in Mode I (tensile) and Mode II (shear) failures at pre-existing joints, i.e. breakages of smooth joint bonds (Yoon et al., 2014). Seismic source parameters are obtained for bond breakage in Mode I, II and also for the subsequent sliding after shear bond breakage, i.e. frictional slip. Bond breakage is treated as a fracturing event and the seismic moment M_0 is computed by a moment tensor M_{ij} (2 by 2 in 2D model) constructed for each bond breakage as show in equation below.

$$M_{ij} = \Sigma\Delta \ F_i R_j \qquad \text{Eq. (3-3)}$$

where ΔF_i is the i-th component of the change in contact force, and R_j is j-th component of the distance between the contact point and the event centroid. The sum is performed over the surface enclosing the event.

Seismic moment is then calculated from the eigenvalues of the moment tensor matrix. Details of this moment tensor can be found in Hazzard and Young (2002 and 2004):

$$M_0 = (\Sigma m_j^2/2)^{1/2} \qquad \text{Eq. (3-4)}$$

where m_j is the j-th eigenvalue of the moment tensor matrix.

Other than fracturing events, slip events occur at pre-existing smooth joints undergo shear slip. The seismic moment M_0 for such slip events is computed by shear modulus G, slip area A and shear displacement d through:

$$M_0 = GAd \qquad \text{Eq. (3-5)}$$

The moment magnitude, M_w, is computed from the seismic moment M_0 (in N·m) by the following equation by Hanks and Kanamori (1979):

$$M_w = 2/3\log M_0 - 6 \qquad \text{Eq. (3-6)}$$

One example of seismicity modelling is shown in Figure 7, where the acoustic emission pattern in the granite sample under asymmetric compressive loading (Zang et al., 2002) is reproduced using the PFC seismicity modelling (Yoon et al., 2012). By using this technique, one could monitor and document the seismic event distribution in time and space as well as the magnitude of the events.

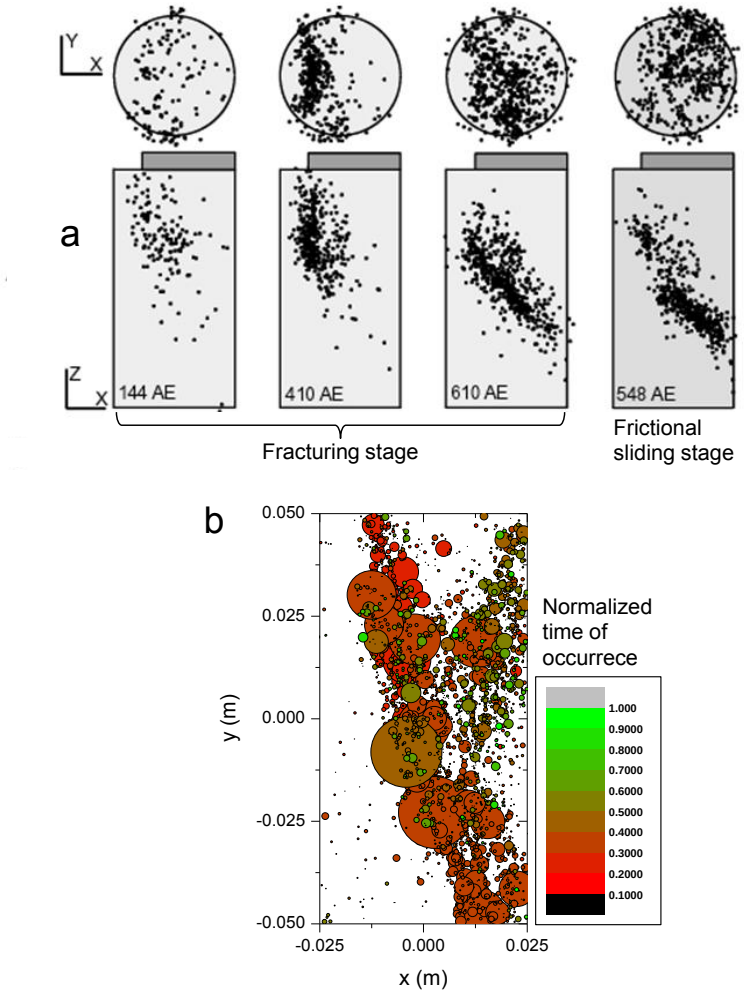

Figure 7. (a) Acoustic emissions observed in the asymmetric compressive test in Aue granite sample (Zang et al., 2002) and (b) seismic events simulated in the clumped particle model (Yoon et al., 2012).

4. Forsmark repository models

4.1. Generation of the horizontal section model of the Forsmark site

4.1.1. Deformation zones

Figure 8 shows the distribution of the two rock domains RFM029 and RFM045, and deformation zones with length larger than 1 km, on a plane at 500 m depth within the Local Model Volume at Forsmark (Stephens et al., 2007). Zones marked in red are steeply dipping or vertical and have a trace length at the surface longer than 3 km. Zones marked in dark green are steeply dipping or vertical and are less than 3 km in length. Zones marked in light green are gently dipping (ZFMA1 and ZFMA2). As displayed by their colours (red and dark green), most of the deformation zones identified by SKB at Forsmark are steeply dipping or vertical.

Figure 9 shows the PFC model representing the Local Model Volume where most of the deformation zones marked in green in Figure 8 are inserted. The model area has been enlarged in order to have additional space at the boundary to remove the side effects that the model boundary can have, e.g. unnecessarily high stress concentration at the tip of the deformation zones being close to the boundary.

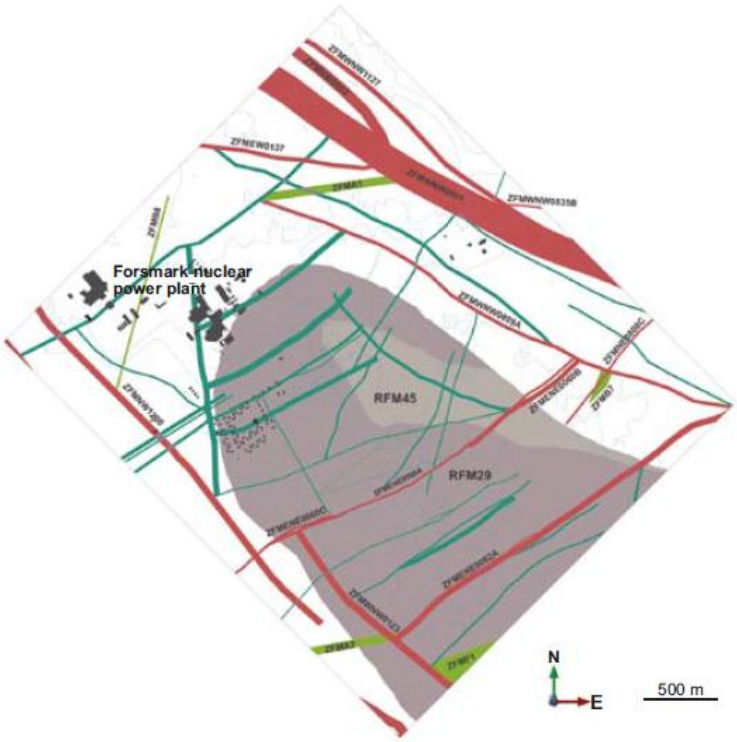

Figure 8. Distribution of the two rock domains RFM029 and RFM045, all deformation zones with length larger than 1 km, projected on a plane at 500 m depth within the Local Model Volume at Forsmark (Figure 5-13 in Stephens et al., 2007).

The generated model does not contain the gently dipping deformation zones (ZFMA1 and ZFMA2), due to technical difficulty in representing gently dipping fracture planes in horizontal sections in PFC. Gently dipping zones are modelled through 2D vertical section models in Sec. 4.2. Another reason for excluding the gently dipping deformation zones in the PFC model is that they are located at a far distance from the repository rock mass from which the effects on the repository stability are estimated negligible.

Table 1 lists the deformation zones included in the horizontal section model and their length (as simulated in the PFC model versus as documented by SKB, Stephens et al., 2007). As indicated by the difference in length, most of the deformation zones in regional-local model scale, except ZFMWNW0809A, are longer than their correspondent in the PFC model. This is due to the fact that the PFC model is limited to the size of the local model area, and the deformation zones extends beyond the size of the local model area are truncated, in particular the zone ZFMWNW0001 (Singö fault).

One should notice that the deformation zone ZFMWNW2225 is elongated by 35% compared to what SKB has documented. SKB has documented that zone is 1613 m long (total trace length at the surface) and truncated by ZFMENE0060A. However, ZFMWNW2225 is modelled so it extends further from ZFMENE0060A and reaches the panel D area. Such measure was taken as the layout D2 by SKB shown in Figure 10b (in particular circled region in the panel D area) does not match the deformation zones documented in Figure 8. Although SKB documented the length of ZFMWNW2225 with high confidence of existence, it was not clear whether there is any missing part of the trace of a deformation zone or another long fracture undetected that explain the empty section in panel D. Therefore, zone ZFMWNW2225 was made longer than SKB in order to be conservative and to have the layout D2 make more sense.

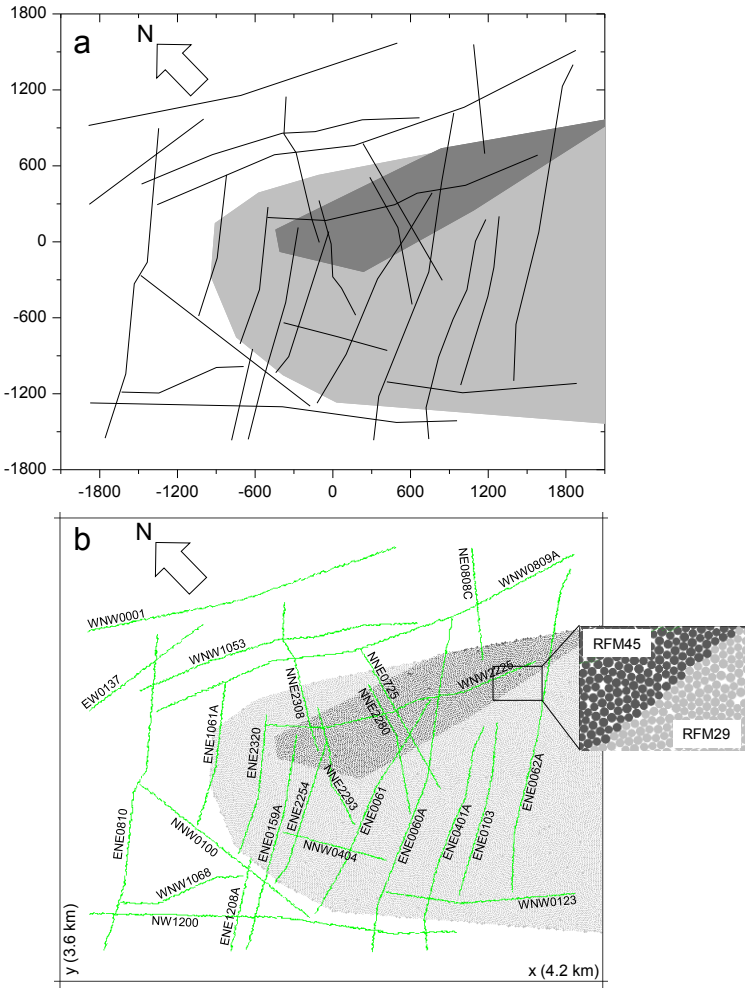

Figure 9. The model generated in PFC for Forsmark consists of three rock domains: RFM045 in dark gray, RFM029 in light gray and the area in white as generic rock mass outside the repository. The repository contains deformation zones with length > 700 m (green).

The insert in Figure 9b shows an enlarged view of a part of one deformation zone. As it can be seen, a deformation zone is not represented as a single planar structure, which is SKB's approach (Fälth et al., 2010), but as a combination of small fracture planes aligned in an echelon structure. The latter approach seems more reasonable as a way of representing deformation zones due to two reasons. The first reason is that fractures and faults (deformation zones) do not usually show perfectly planar structures. As SKB mentioned, irrespective of the surface roughness observed in the laboratory, fractures may be undulated or stepped on the large scale (Fälth et al., 2010). The second reason is that SKB has observed and documented that the deformation zones have large variations of thickness (see Appendix 15 in Stephens et al., 2007). By representing a deformation zone through stepped alignment makes it possible to create the large spans of thickness closer to reality.

Table 1. Deformation zones included in the Forsmark horizontal section model and comparison of the length (modelled vs. documented by SKB).

Deformation zone	Modelled length (m)	Documented length[1] (m)	Difference[2] (%)	Remarks
ZFMWNW0809A	3,482	3,347	4	Regional and local
ZFMNW1200	2,842	3,121	9	Regional and local
ZFMWNW0123	1,475	5,086	71	Regional and local
ZFMENE0062A	2,552	3,543	28	Regional and local
ZFMENE0060A	2,676	3,120	14	Regional and local
ZFMWNW0001	2,476	30,000	92	Regional and local (truncated Singö fault)
ZFMEW0137	1,110	4,300	74	Regional and local
ZFMNNW0100	1,665	1,673	0	Local
ZFMENE0810	2,506	2,672	6	Local
ZFMENE0061	1,889	2,081	9	Local
ZFMENE0103	1,369	1,399	2	Local
ZFMENE0159A	1,720	1,909	10	Local
ZFMNNE0725	1,242	1,274	3	Local
ZFMENE1061A	1,140	1,158	2	Local
ZFMWNW1053	2,231	2,686	17	Local
ZFMWNW2225[3]	2,178	1,613	35	Local
ZFMENE2320	1,109	1,251	11	Local
ZFMENE2254	1,198	1,021	17	Local
ZFMNE0808C	868	1,156	25	Regional and local
ZFMNNE2280	1,069	1,035	3	Local
ZFMNNE2308	1,202	1,419	15	Local
ZFMNNE2293	9,68	996	3	Local
ZFMENE0401A	1,813	1,961	8	Local
ZFMNNW0404	830	947	12	Local
ZFMWNW1068	986	999	1	Local
ZFMENE1208A	739	1,081	32	Local

[1] Appendix 15 in Stephens et al. (2007)

[2] Relative difference (%) = |documented-modelled|/documented x 100

[3] This deformation zone is enlarged in length to make the layout D2 make sense.

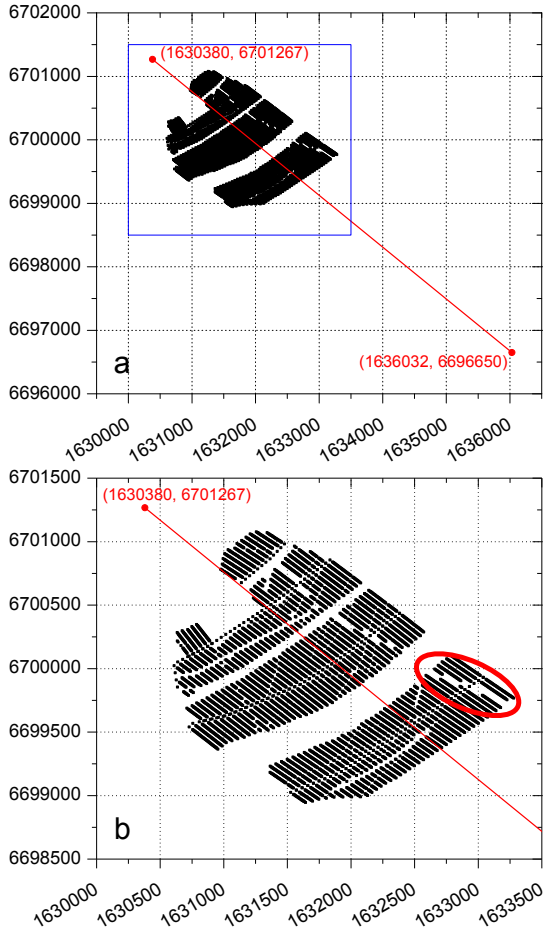

Figure 10. Canister deposition position in the layout D2. (a) NW-SE profile along candidate volume (see also Figure 15) is shown by the red line; (b) detail of the layout D2 in relation to zone ZFMWNW2225.

4.1.2. Discrete Fracture Network (DFN)

For the fracture network in the repository, ten realizations of DFN were created (see Appendix 2). Among the realizations, DFN03h and DFN06h are selected for the modelling as shown in Figure 11. Distributions of length and orientations of the fractures are shown in Figure 12 and 13, respectively, which show similar patterns.

Coulomb Failure Stress (*CFS*) on each of the fractures is calculated and the histograms are shown in Figure 14. The histograms are fitted with the Gaussian distribution and the mean values are indicated. As positive value of *CFS* means that the fracture is close to frictional failure. Realization DFN03h is chosen as the most conservative realization while DFN06h as the least conservative.

Figure 11. Horizontal section of the models with realizations (a) DFN03h, the most conservative case, and (b) DFN06h, the least conservative from a frictional point of view.

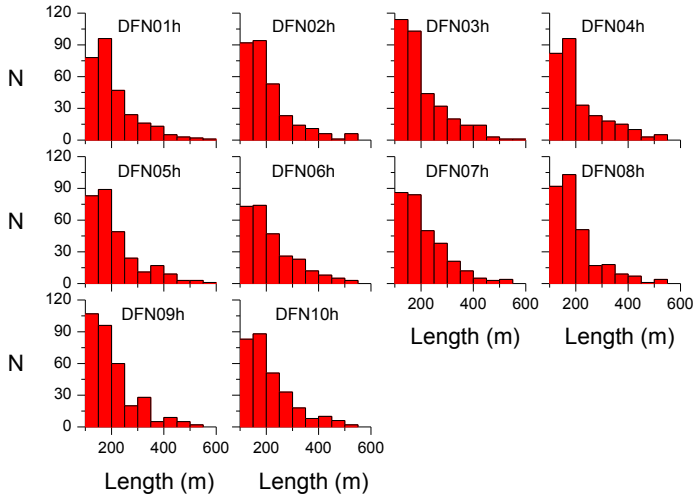

Figure 12. Frequency distribution of the fracture lengths in ten DFN realizations.

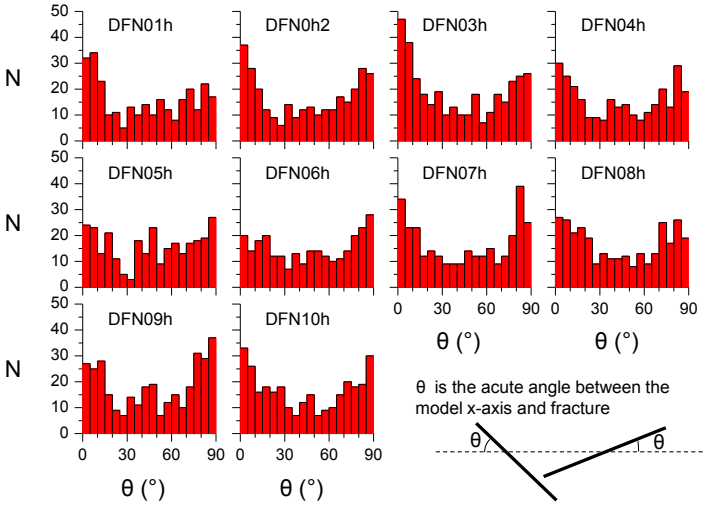

Figure 13. Frequency distribution of the fracture orientations with respect to model x-axis in ten DFN realizations.

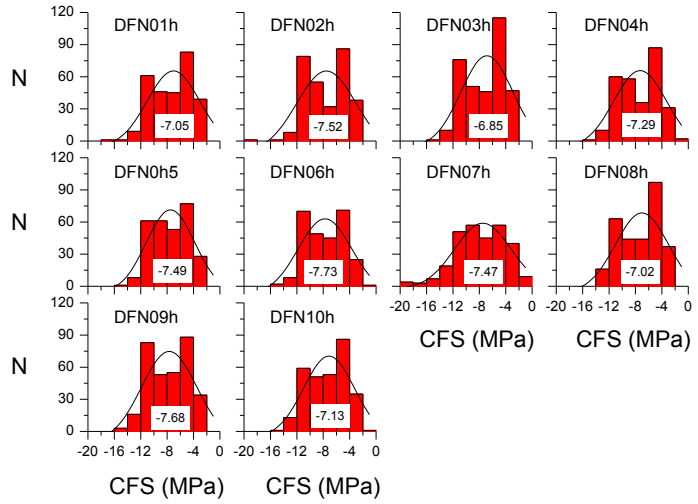

Figure 14. Frequency distribution of *CFS* of the fractures in ten DFN realizations. Numbers in each figure are the mean value of the *CFS* of the Gaussian distributions fitted to the histograms.

4.2. Generation of the vertical section model of the Forsmark site

Figure 15a shows a NW-SE cross section through the Candidate Volume in the structural model containing rock domains and deformation zones at Forsmark (Figure 4-12 in SKB, 2011). From this figure, the vertical cross section model is constructed as shown in Figure 15b. Table 2 lists the deformation zones embedded in the vertical section model and their lengths. However, unlike in Table 1, comparison was not made with the SKB's documented lengths as the documented length is the trace length of the deformation zones on the ground surface, not along a vertical section. The rock domain RFM032 is modelled as a rock domain rather than as a deformation zone to mimic the "tectonic lens" at Forsmark.

Figure 16 shows the vertical cross section models where two cases of DFN realizations are implemented, DFN03v and DFN06v as in Sec. 4.1.2 and Figure 11. Those discrete fractures with trace length smaller than 125 m and those that do not intersect the repository horizon at 500 m depth are removed from the original DFN sets which are shown in Appendix 2.

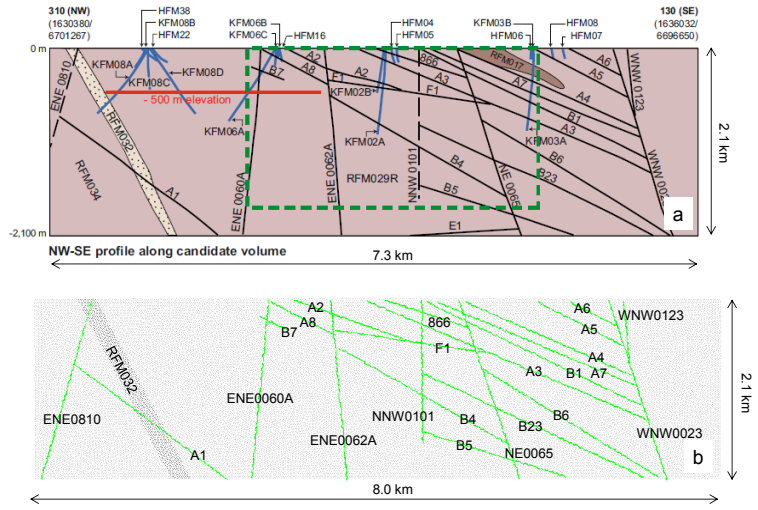

Figure 15. (a) NW-SE cross section through the Candidate Volume in the structural model showing rock domains and deformation zones (Figure 4-12 in SKB, 2011) and (b) vertical section model of Forsmark. The location of the vertical cross section is shown in Figure 10.

Table 2. Deformation zones included in the vertical cross section PFC model of Forsmark.

Deformation zone	Modelled length (m)	Deformation zone	Modelled length (m)
ZFMA1	2,225	ZFMB6	2,392
ZFMA2	1,340	ZFMB7	371
ZFMA3	3,537	ZFMB23	2,842
ZFMA4	2,115	ZFMF1	1,825
ZFMA5	1,096	ZFM866	1,014
ZFMA6	593	ZFMENE0810	2,513
ZFMA7	2,491	ZFMENE0060A	2,080
ZFMA8	834	ZFMENE0062A	2,091
ZFMB1	2,771	ZFMNNW0101	1,663
ZFMB4	2,224	ZFMNE0065	2,189
ZFMB5	1,758	ZFMWNW0023	2,190
		ZFMWNW0123	714

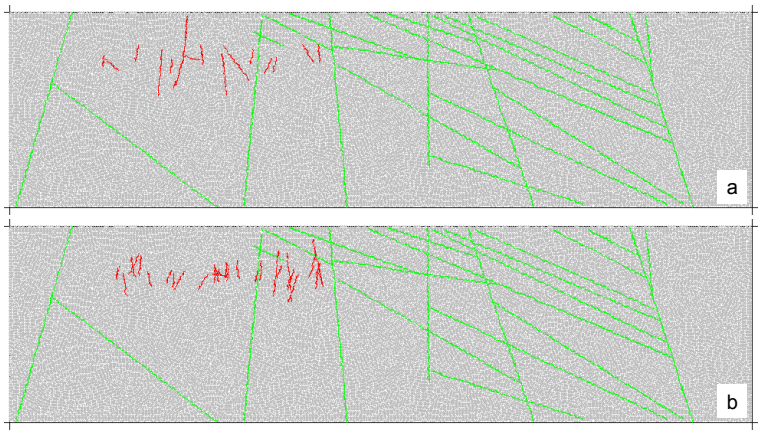

Figure 16. Vertical section model of Forsmark with deformation zones in green and embedded DFN fractures in red for realization (a) DFN03v and (b) DFN06v. Fractures shorter than 125 m that do not intersect the repository horizon are not considered in the model. Original DFN sets can be found in Appendix 2.

4.3. Model parameters

Table 3 shows the parameters used for the rock mass domains, deformation zones and target fractures. In addition to these parameters, other modelling parameters for the seismicity computation have been used. For each of the parameters related references are given in the table. For the rock mass domains, the rock mass parameters are used because of the high threshold for the shortest fractures in the model of 125 m. For the target fractures, the mechanical properties of the rock fractures from domain FFM01 are adopted (Table 4).

Table 3. Mechanical and thermal model parameters for the rock mass.

Parameter (unit)	Value	Reference/Remark
Density (kg/m^3)	2700	Hökmark et al. (2010)
Deformation modulus (GPa)	70	Glamheden et al. (2007)
Poisson's ratio	0.23	Glamheden et al. (2007)
Tensile strength (MPa)	2.3	Glamheden et al. (2007)
Cohesion (MPa)	27	Glamheden et al. (2007)
Friction angle (°)	50	Glamheden et al. (2007)
Thermal conductivity (W/m-K)	3.57	Hökmark et al. (2010)
Linear thermal expansivity (1/K)	7.7e-6	Hökmark et al. (2010)
Specific heat (MJ/m^3-K)	2.06[1]	Hökmark et al. (2010)

[1] The specific heat is in unit of MJ/(m^3-K) which is volumetric heat capacity. The value is adjusted to mass specific heat capacity 792.96 in unit of J/(kg-K) as this is the unit required for input to the PFC thermal analysis.

Table 4. Model parameters for the target fractures.

Parameter (unit)	Value	Reference and remarks
Shear stiffness, *K*s (GPa/m)	34	Hökmark et al. (2010)
Normal stiffness, *K*n (GPa/m)	656[1]	Hökmark et al. (2010)
Friction angle (°)	35.8	Hökmark et al. (2010)
Dilation angle (°)	3.2	Hökmark et al. (2010)
Tensile strength (MPa)	0	Hökmark et al. (2010)
Cohesion (MPa)	0.5	Hökmark et al. (2010)

[1] The normal stiffness 656 GPa/m is obtained from testing of laboratory scale sample. For input to the smooth joint normal stiffness, this value is adjusted using the scaling relation by Morris et al. (2013): *K*n (MPa/mm) = 7420×$L^{-0.631}$, *L* is average particle diameter in the model (in cm).

4.4. Calculation of shear displacements of fractures

This section describes how the shear displacement of a single fracture is calculated. As mentioned earlier in Sec. 4.1, a single line fracture (joint) is represented as a collection of small length segments consisting of smooth joint elements. This is illustrated in Figure 17. Such representation of a fracture might be more reasonable than straight lines as fractures in nature do not show perfectly planar structures and, irrespective of the surface roughness observed in laboratory, fractures may be undulated or stepped at large scale (Fälth et al., 2010).

The main output of the modelling conducted in this study is the shear displacement of the target fractures due to thermal and earthquake loadings. For calculation of the shear displacement of a fracture that is represented by a collection of smooth joint, a representative value should be calculated. Figure 18 shows the distribution of shear displacement of fractures with respect to their trace length. Shear displacements values shown in black are calculated as the sum of the shear displacement of all the smooth joints constituting a single fracture, whereas those shown in red are calculated as the average of the smooth joints shear displacements. When displacements are summed, the representative shear displacement of a fracture is overestimated. The longer the fracture, the larger the sum of the shear displacements since more smooth joints constitute the fracture. Therefore, shear displacements of the smooth joints are averaged and used as a representative displacement for the whole target fracture.

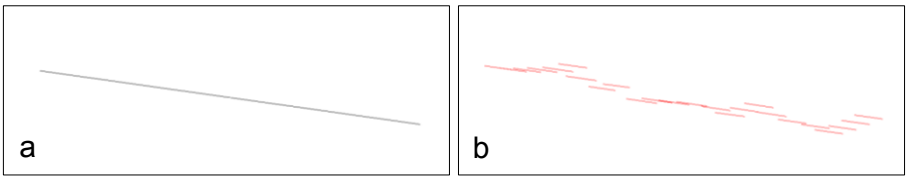

Figure 17. Conversion of (a) a single planar joint to (b) a collection of smooth joints.

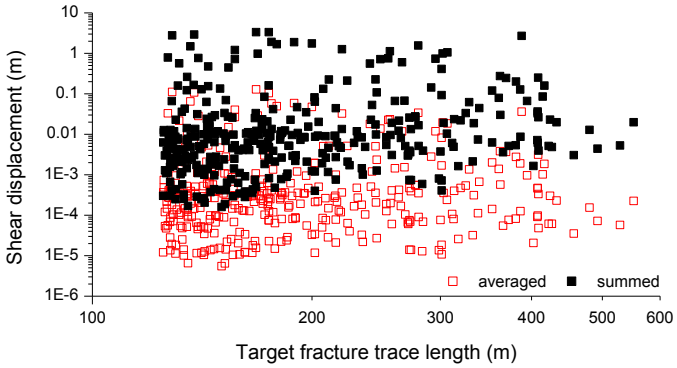

Figure 18. Distribution of shear displacement of target fractures calculated by summing the shear displacements of smooth joints (in black) and by averaging the shear displacements of smooth joints (in red) with respect to fracture length.

4.5. In situ stress field and its glacial evolution

One in situ stress field is investigated for the horizontal section model. The reverse stress field defined as “most likely” by SKB is used in this study. The maximum horizontal stress is SH = 40 MPa and the minimum horizontal stress is Sh = 22 MPa at the repository depth (Martin, 2007; Glamheden et al., 2007) as shown by the solid lines in Figure 19. The maximum horizontal stress SH is oriented at N145°E.

The in situ stress field might evolve during next glacial cycle based on a reconstruction of the Weichselian glaciations. For the purpose of the modelling work, only two points in time, the major advance and retreat of the ice cover are considered. Based on the modelling results by Lund et al. (2009), glacially induced stress increments (ΔSH, ΔSh and ΔSV) are calculated for the selected times indicated in Figure 20. One is at time of forebulge (gis1) after the first glacial maximum. The second is at time of maximum thickness of ice cover (gis2). The stress increments at the two selected times are read from the curves and added to the present day most likely stresses. Therefore, at time of forebulge, the resulting SH and Sh are 40 and 17 MPa, respectively. At time of maximum thickness of ice cover, the resulting SH and Sh are 55 and 35 MPa, respectively. At both times it is assumed that the orientation of SH is unchanged and equal to N145°E.

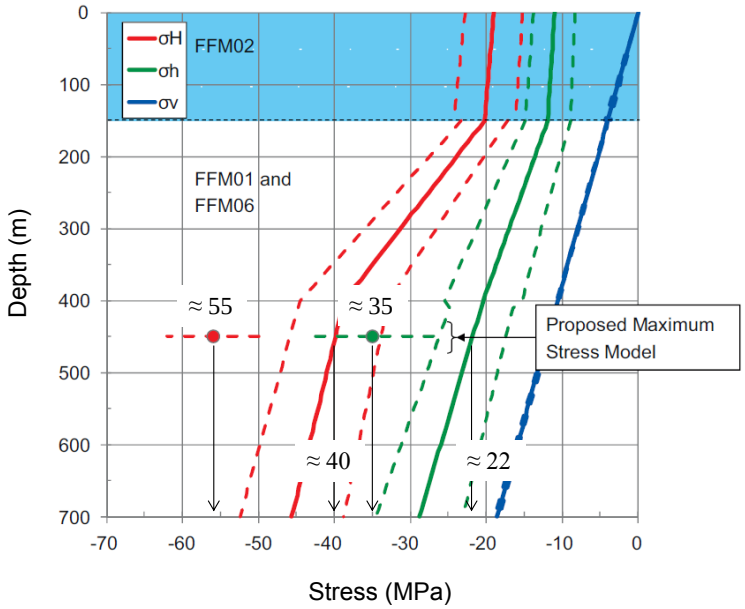

Figure 19. In situ stress model “most likely” with associated uncertainty spans (Glamheden et al., 2007) for the region around the target area at Forsmark.

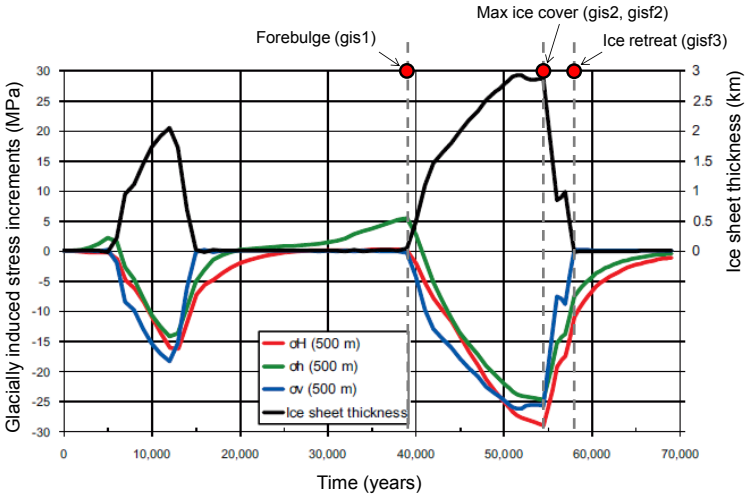

Figure 20. Glacially induced principal stress increments (ΔSH, ΔSh, ΔSV) at the repository depth during the future glacial cycle (modified from Hökmark et al., 2010). Two time points are selected and applied to the horizontal section model (gis1, gis2) and the vertical section model (gisf2, gisf3).

The Forsmark model is constructed using SKB's local model area that is oriented at N135°E. As the orientations of the SH is N145°E, it was necessary to adjust the boundary conditions with shear stresses to take into account the 10° deviation. The magnitude of such shear and normal stresses are computed by the Mohr circle plots shown in Figure 21. This was achieved by controlling the velocity of the boundary layer particles which are shown in orange in Figure 22. Figure 22 shows the horizontal section models with three different sets of stresses applied as boundary conditions: (a) and (d) present-day "most likely", (b) and (e) glacially induced at time of forebulge, (c) and (f) glacially induced at time of maximum thickness of the ice cover. The DFN03h (left column) and to the DFN06h (right column) realizations were analysed with PFC. In summary, Table 5 lists the principal stresses (SH and Sh) that are achieved in the horizontal section models for different boundary stress fields. The boundary layer (in orange in Figure 22) also serves as a barrier that prevents the seismic energy and waves from reflecting backward to the model. This is done by assigning high level of viscous damping so that the seismic wave dies out substantially when it reaches and passes the viscous damped boundary layer (Yoon et al., 2014).

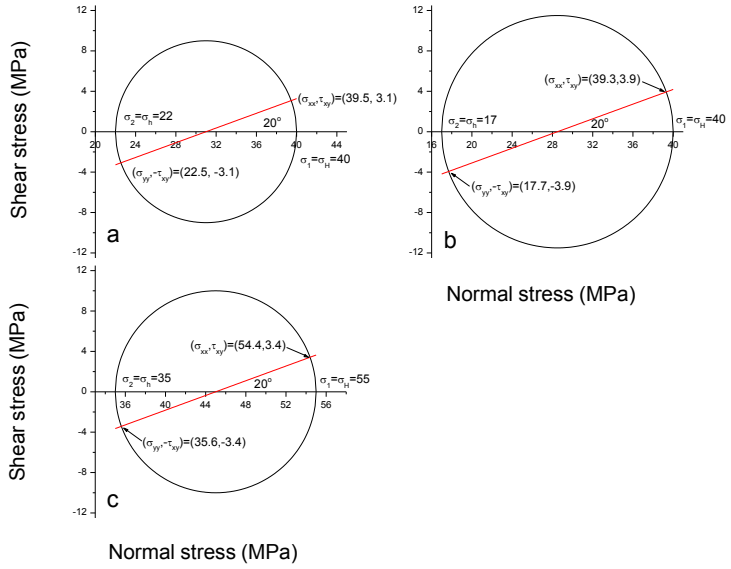

Figure 21. Mohr circle plots for calculation of boundary stress components (σ_{xx}, τ_{xy}, σ_{yy}) to achieve required principal stresses for different initial stress models: (a) present-day "most likely" stress, (b) glacial induced stress at time of forebulge, (c) glacial induced stress at time of maximum thickness of ice cover. Bisecting the indicated angle gives the deviation of SH from the model x-axis, which corresponds to N135°E.

Table 5. Stress components (SH and Sh) in different initial stress fields applied to the horizontal section model.

Stress fields (coded name)	SH, Sh (MPa)	SH orientation	Reference
Initial most likely stress "most likely" (mls)	40, 22	N145°E	Martin (2007)
Glacial induced, forebulge (gis1)	40, 17	N145°E	Hökmark et al. (2010)
Glacial induced, max. ice cover (gis2)	55, 35	N145°E	Hökmark et al. (2010)

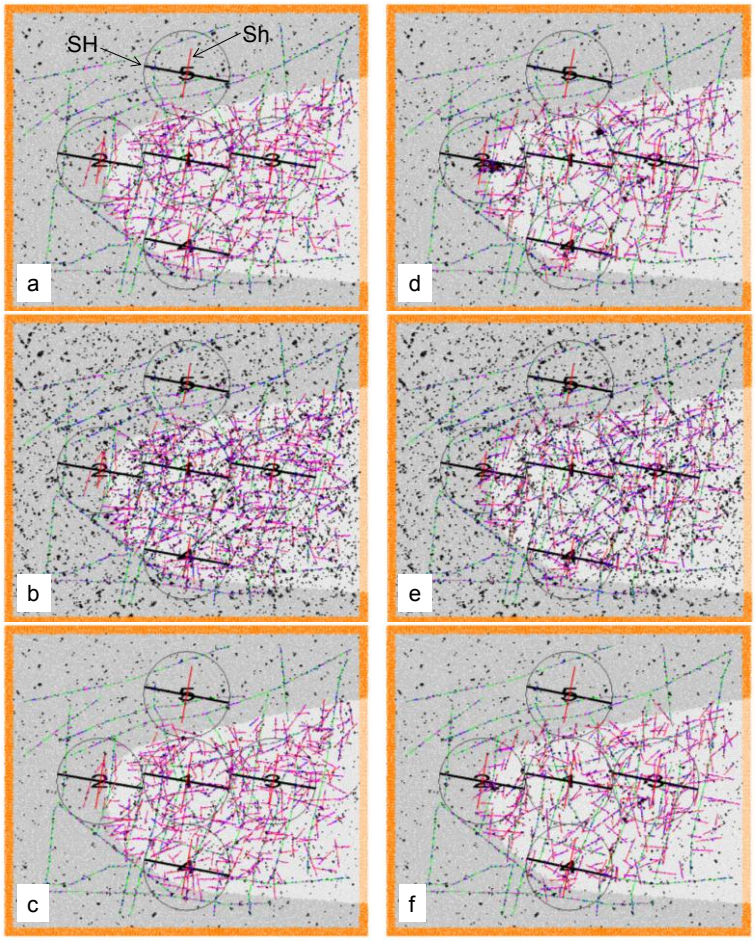

Figure 22. Forsmark horizontal section models in equilibrium under various stress fields: (a, d) present day most likely, (b, e) glacial induced at time of forebulge, (c, f) glacial induced at time of max ice cover. Left and right column show the most and the least conservative cases of DFN realizations (left: DFN03h, right: DFN06h). Five regions are selected for local monitoring of the evolution of the principal stresses (SH and Sh), of which the orientations are indicated by the black and red lines in the circles.

Table 6. Stress components (SH and SV) at the repository depth in different stress conditions applied to the vertical section model.

Stress models (coded name)	SH (MPa)	SV (MPa)	Reference
Initial most likely stress “most likely” (mls)	40	12.5	Fälth et al. (2010)
Glacial induced stress field, max. ice cover (gisf2)	55 (+15)[1]	26.5 (+14)[2]	
Glacial induced stress field, ice retreat (gisf3)	52.5 (+12.5)[1]	12.5 (+0)[2]	

[1] Stress increment to the present day maximum horizontal stress due to glacial effect, which is read from Figure 20.

[2] Stress increment to the present day vertical stress due to glacial effect, which is read from Figure 20.

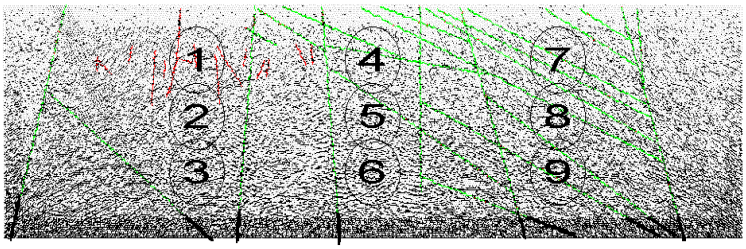

Figure 23. Forsmark vertical section model subjected to reverse stress field and locations of local stress measuring area. Compressive contact force is represented in black with thickness scaled to the magnitude.

Stress components (SH and SV) that are achieved in the vertical section models are shown in Table 6. Numbers in parentheses are the stress increments that are added to the stress components of the present-day "most likely" reverse stress field.

Gradients of stress with depth for SH and SV are calculated from Eq. (7-4) in Fälth et al. (2010), which yield 0.078 MPa/m and 0.026 MPa/m for SH and SV, respectively. Ratio of stress, k = SH/SV, is kept equal to 3 for the entire depth range.

Figure 23 shows the Forsmark vertical section model where the reverse stress field is implemented. Stress measurement areas are chosen in the model to monitor the locally evolving stresses. For the monitoring of the stresses (σ_{xx}, τ_{xy}, σ_{yy}), the Authors used "measurement circle" logic of PFC. Stress is a continuum quantity. Therefore does not exist at each point in a particle assembly because the medium is discrete. In the measurement circle logic in PFC model, contact forces and particle displacements are computed, and averaging procedures are done to make the step from the microscale (i.e. contact point quantities) to a continuum (i.e. area or volume averaged quantities). Principal stresses (SH and Sh for the horizontal section model, and SH and SV for the vertical section model) are then computed from the measured stresses (σ_{xx}, τ_{xy}, σ_{yy}).

After the stress field is applied, the locally monitored stresses (SH and SV) are compared to the stress gradients for the reverse stress field (Figure 24a), glacial induced stresses at time of maximum thickness of ice cover (Figure 24b) and at time of ice cover retreat (Figure 24c).

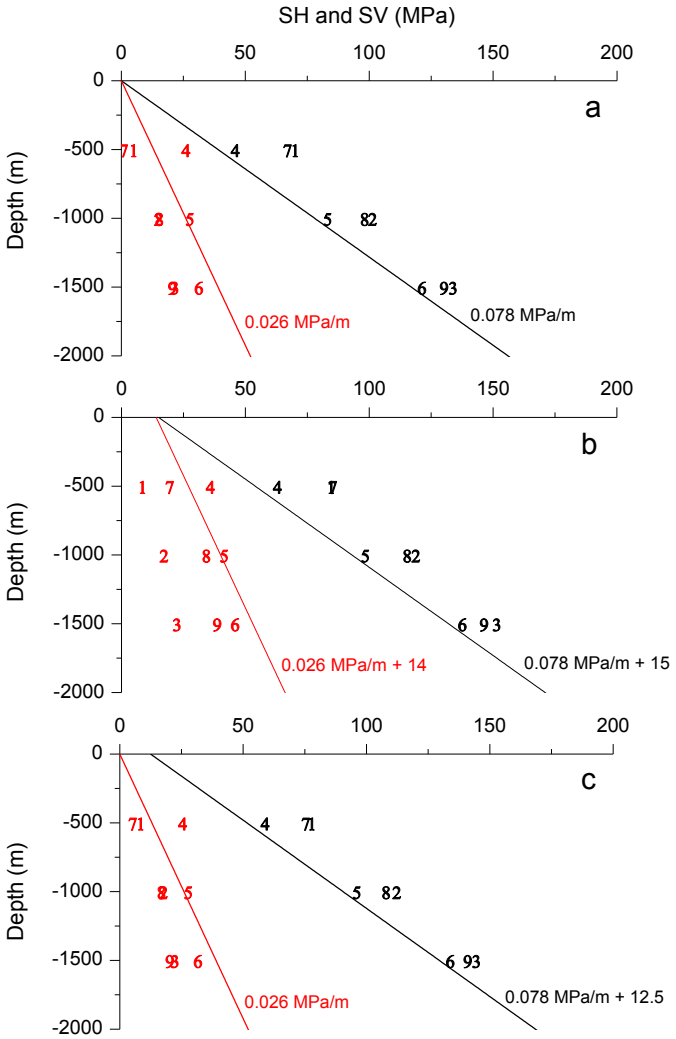

Figure 24. Stress components (SH in black and SV in red) monitored by the local stress measurement area located at selected depth (500, 1000 and 1500 m), and gradients of SH and SV for: (a) the reverse stress “most likely” field, (b) glacial induced stress field at time of maximum thickness of ice cover, (c) glacial induced stress field at time of ice cover retreat.

4.6. Heat loading

For the analysis of target fracture responses induced by the heat from the canisters containing spent nuclear fuel, a group of particles are assigned as point sources (i.e. deposition holes with spent fuel canisters or "equivalent canisters") that generate heat to the surrounding particles through their contacting points (see Sec. 3.4 for theory of thermal analysis in PFC).

Figure 25 shows the locations of the canister deposition holes in the realizations DFN03h and DFN06h, where no canisters are emplaced in relation to fractures intercepting the full perimeter of the deposition tunnel. Black dots are the canister deposition holes in the panel A. Red, green and blue dots are the canister deposition holes in the panel B, C, and D, respectively. It should be noted that the rule of 6 m to 6.8 m spacing between the deposition holes assigned by SKB was not met due to the particle density in the model. Ideally, particle diameter should be small enough to be equivalent to the size of the deposition hole diameter (i.e. 1.75 m). However, packing the model with area of 15.12 km^2 (3.6 km × 4.2 km) with particles having average diameter of 1.75 m requires a few million particles, which makes the simulation practically impossible.

In order to simulate the heat generated from the spent fuel canisters, a normalized thermal power curve $P(t)$ (Hökmark et al., 2010) and the initial thermal power of a single canister are used. For layout D2, a canister is assumed to have initial power of 1700 W (Hökmark et al., 2009). Therefore the decay function of the heat power of a canister is expressed as:

$$Q(t) = 1700 \times P(t) \text{ W} = 1700 \times \Sigma[a_i \times \exp(-t/t_i)] \text{ W} \qquad \text{Eq.(4-1)}$$

where, a_i are coefficients that define how the thermal power decays (Hökmark et al., 2010) and are shown in Figure 26. Decay coefficients a_i and t_i are identical to the SKB's reference fuel (Hökmark et al., 2009). Figure 26 shows canister power decay of BWR and PWR fuel for two interim storage assumptions. The BWR and PWR data are from Hökmark et al. (2009).

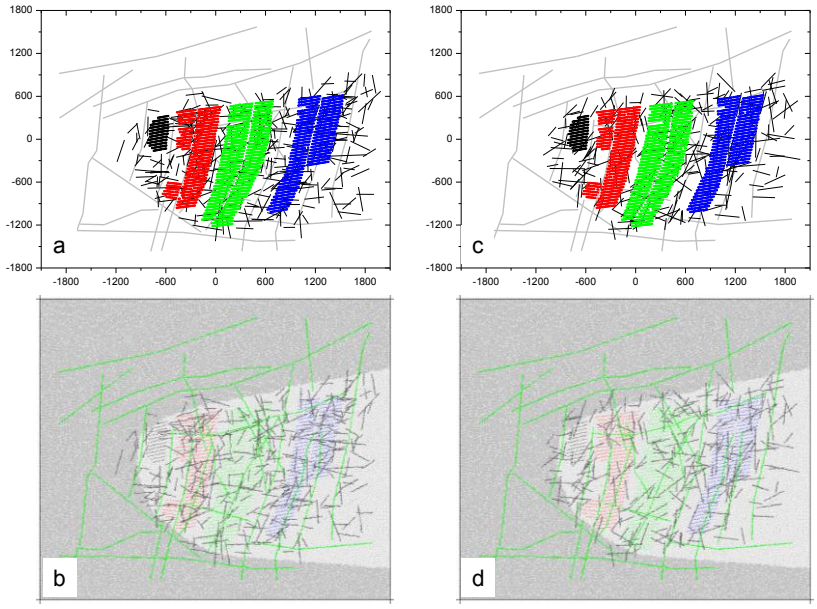

Figure 25. Location of the canister deposition holes in (a) DFN03h and (c) DFN06h realizations. Bottom figures show distribution of particles that act as point heat sources (panel A in black, panel B in red, panel C in green, panel D in blue).

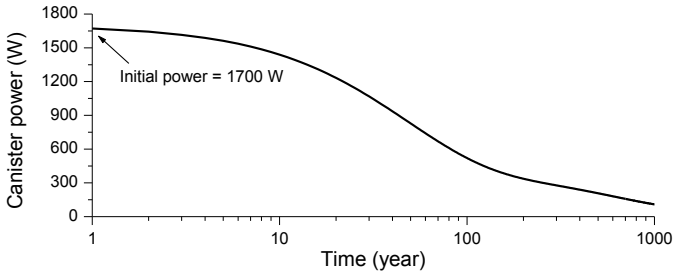

Figure 26. Decay of canister heat power with time, from the normalized heat power curve of 35 and 40 year-old BWR and PWR fuel with burn-up 38 MWd/kgU and 60 MWd/kgU.

The rock temperature $T(t)$ at the wall of the deposition hole is used as a direct input to the heat source particles (equivalent canisters). The $T(t)$ is computed by a combination of initial wall rock temperature T_{ini} and the temperature drop $\Delta T(t)$ across the bentonite buffer in dry and wet deposition holes (Hökmark et al., 2010). For the modelling, all deposition holes are assumed to be dry.

Two modelling cases of repository rock mass heating are considered here. Table 7 lists the number of canister in each panel and the starting times of heat release that are calculated according to the rule of "deposition of 1 canister per 3 days". It should be noted that the number of canisters in each panel is dependent on the DFN patterns adopted. The locations of the deposition holes are calculated by means of the Full Perimeter Intersection criteria (FPI, Munier, 2010).

In the realization DFN03h, panel A contains 310 equivalent canisters. The heating of the panel starts at about 2.5 years. As it takes 12 years (1456 canister × 3 days/canister × 1 year/365 days = 12 years) to dispose the canisters in panel A, the start time of heating of panel B is 14.5 years (2.5+12). The same logic applies to the start time of heating of panel C and D, and for realization DFN06h (Table 8). Figure 27 shows four curves describing how the temperature at the wall of the deposition hole in panels A to D decays with time in realization DFN03h (Figure 27b) and in DFN06h (Figure 27c). These temperature decay curves define the sequential heat loading. For the simultaneous heat loading, all canisters are disposed at the same time (Figure 27a).

Table 7. Number of equivalent canisters in the panels and estimated start time of heat release for the case of sequential deposition for realization DFN03h.

Panel	No. of canisters	Time needed for deposition (years)	Start time of heat release (years)
A	310	2.5	2.5
B	1456	12.0	14.5
C	2263	18.6	33.1
D	1815	14.9	48.0
Total	5844		

Table 8. Number of equivalent canisters in the panels and estimated start time of heat release for the case of sequential deposition for realization DFN06h.

Panel	No. of canisters	Time needed for deposition (years)	Start time of heat release (years)
A	309	2.5	2.5
B	1467	12.1	14.6
C	2265	18.6	33.2
D	1808	14.9	48.1
Total	5849		

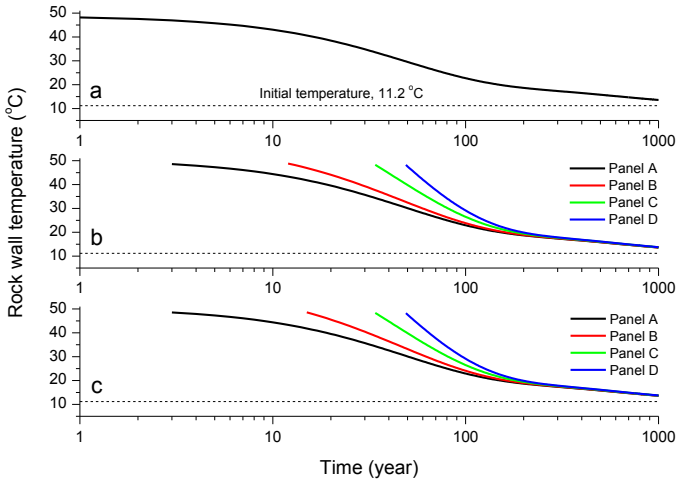

Figure 27. Rock temperature curves at the walls of deposition holes in panels A to D. The curves are assigned to the heat source particles as initial temperature conditions: (a) simultaneous heating, (b) sequential heating for realization DFN03h, and (c) sequential heating for realization DFN06h.

4.7. Stability of the deformation zones

For each of the initial in situ stress models proposed by SKB, the stability of the deformation zones is evaluated using the stability quantity *CFS* (Coulomb Failure Stress) which is defined as:

$$CFS = \tau - \mu \times (\sigma_n - P_f) - c \qquad \text{Eq. (4-2)}$$

where τ and σ_n are the shear and normal stresses, respectively, acting on a smooth joint plane, P_f is the pore pressure, μ is the coefficient of friction, and c is the cohesion. Positive values of *CFS* indicate instability (Fälth et al., 2010).

Figure 28 shows the calculated *CFS* values of the deformation zones under the present day "most likely" stress conditions (Martin, 2007). Mean and standard deviation of the *CFS* of a deformation zone are calculated by the individual *CFS* of the smooth joints that constitute the deformation zone. The dots presented in the figures are mean values and the standard deviations are marked by the error bars.

In general, those deformation zones with smaller trace length, e.g. ZFMENE2254, ZFMNNE2280, ZFMNNE2308, ZFMNNE2293, and ZFMWNW1068, are showing larger standard deviations. This is due to the fact that relatively shorter trace lengths are represented by a few shorter linear joint segments, which can result in wider range of uncertainty of the computed *CFS*.

SKB's estimates (Fälth and Hökmark, 2013) are marked by the grey symbols. The figure indicates that deformation zones ZFMWNW0809A, ZFMNW1200 and ZFMWNW0123 can be considered unstable in both the Author's and SKB's analysis due to the high values of *CFS*.

Figures 29 and 30 show the *CFS* values of the deformation zones under glacial induced stress condition at time of forebulge (gis1) and at time of maximum thickness of ice cover (gis2), respectively.

In all three tested stress conditions, 10 deformation zones can be estimated to be unstable: ZFMWNW0809A, ZFMNW1200, ZFMWNW0123, ZFMWNW0001, ZFMEW0137, ZFMNNW0100, ZFMWNW1053, ZFMWNW2225, ZFMNNW0404, ZFMWNW1068. Almost all of them are oriented NW-NNW-WNW. Among these, four are selected for the earthquake modelling: ZFMWNW0809A, ZFMWNW0001, ZFMWNW2225, ZFMNW1200 (indicated by the red stars in Figure 28 to 30).

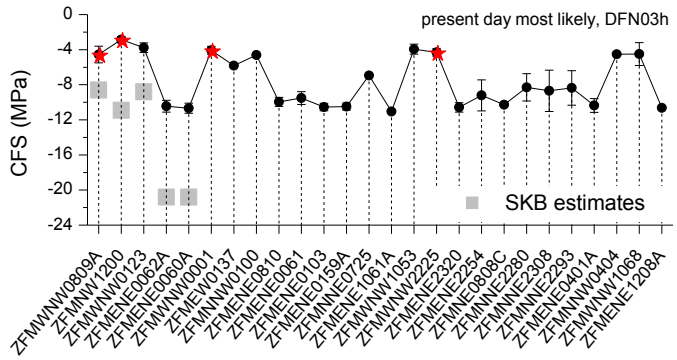

Figure 28. *CFS* values (mean and standard deviation) of the deformation zones determined in this study under present-day "most likely" stress field (Martin, 2007). SKB's estimates of *CFS* (Fälth and Hökmark, 2013) are plotted by means of grey symbols.

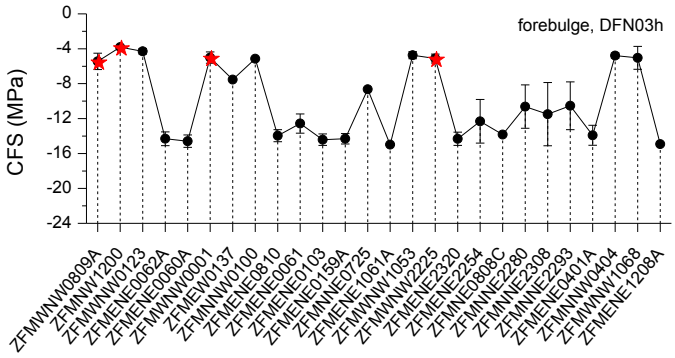

Figure 29. *CFS* values (mean and standard deviation) of the deformation zones under glacial induced stress field at the time of forebulge.

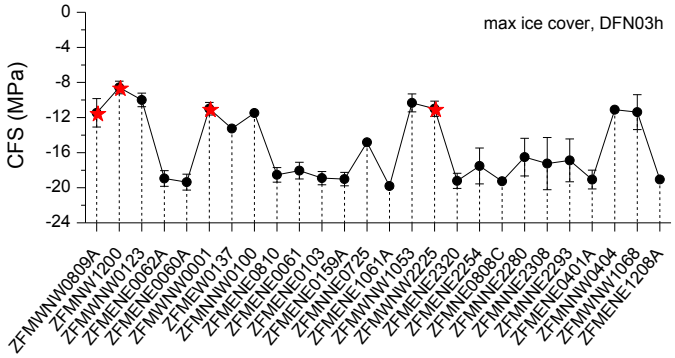

Figure 30. *CFS* values (mean and standard deviation) of the deformation zones under glacial induced stress field at the time of maximum thickness of ice cover.

4.8. Earthquake simulations

Earthquake at a specific deformation zone is simulated by releasing the stored strain energy under a given stress condition at the smooth joint contacts that belong to an earthquake hosting deformation zone. In order to build up strain energy and store it in the trace of a deformation zone, the bond strength of the smooth joint contacts at the deformation zone is multiplied by a factor of 1000. Thereafter the model is compressed using a servo-controlled routine to reach the target principal stresses (SH and Sh in Table 5 for the horizontal section model, and SH and SV in Table 6 for the vertical section model). Deformation and failure of the other smooth joints in the model (other deformation zones and target fractures) are allowed.

For the earthquake modelling of the horizontal section model, four deformation zones are considered unstable: ZFMWNW0809A, ZFMWNW0001, ZFMWNW2225, ZFMNW1200, which are shown red in Figure 31. For the vertical section model (Figure 32), two cases are considered where a single zone ZFMA2 is activated under the given stress field, and a second case where multiple zones ZFMA2, ZFMA3, ZFMA8, and F1 are activated at the same time.

The release of the stored strain energy is simulated by lowering the bond strength of the smooth joint contacts along the active deformation zone with a multiplication factor 10^{-20} to the tensile and cohesion strength of the smooth joints. In addition to this, friction and dilation angles of these smooth joint are lowered to 10% of their original values, i.e. from 35° to 3.5°. Such measure was taken to mimic a rupture process and strain energy release when fracture surface asperities are broken by the earthquake slip. Lowering of the normal and shear stiffness of the smooth joints was not considered because of its minimal impact on the rupture process.

In addition to lowering of the bond strength, shear forces acting on the smooth joints are powered by a force multiplication factor. This measure was taken to power up the shear force, therefore to increase the shear displacement of the smooth joints. This results in an increase of the magnitude of a generic earthquake. However, this technique is used in a few modelling cases, which is indicated in the section heading with “powered shear force”.

In all earthquake modelling cases, the moment magnitudes of the simulated earthquakes, which are a direct output of the PFC modelling, correspond to the seismic energy released at the earthquake hosting deformation zones with 1 m width in the out-of-plane direction. Therefore, it can be said it correspond to a work per meter (Nm/m or J/m). This is due to 2D nature of PFC where the model is set to have 1 m unit thickness in the out-of-plane direction. This makes the magnitude directly obtained from PFC far underestimated. To overcome this problem, it is assumed that the deformation zones have an out-of-plane width equal to their length, i.e. rupture area RA = length × width = $(\text{length})^2$. The simulated seismic moment M_0 (Nm/m) is then multiplied by the width (equal to the length) of the deformation zone in order to take into account of its full size. The seismic moments (M_0) that correspond to the full size deformation zones are then converted to moment magnitudes (M_w) using Eq. (3-6).

In some of the earthquake modelling cases, activation of a deformation zone yields multiple hypocentres as deformation zones are represented by a combination of several linear segments as shown in Figure 9. In such case, arithmetic means of the coordinates of the multiple hypocentres are used for the coordinate of a representative earthquake hypocentre with average magnitudes.

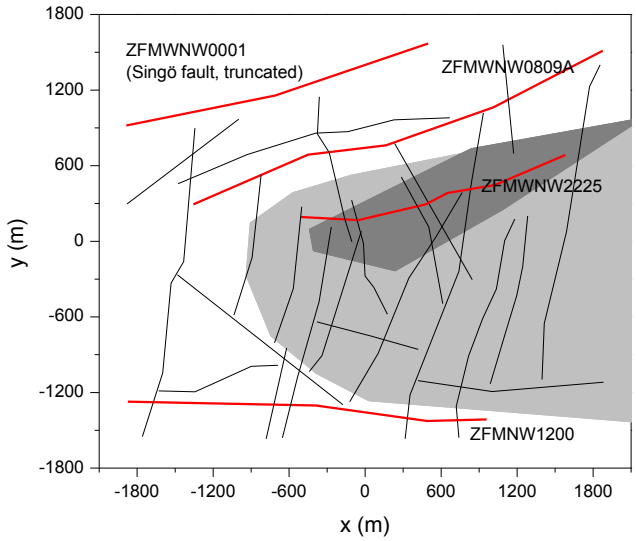

Figure 31. In red, the deformation zones selected for earthquake modelling in the horizontal section model.

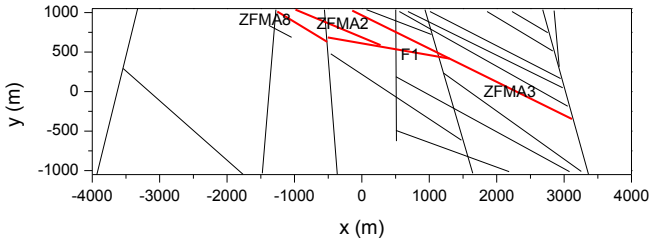

Figure 32. In red, the deformation zones selected for earthquake modelling in the vertical section model.

Figure 33 is a detail view of the PFC modelling that shows earthquake seismic events generated by releasing the stored strain energy at the smooth joint contacts belonging to zone ZFMWNW0809A. The ellipse represents single seismic event with magnitude scaled to the size of the ellipse and its centre represents the hypocentre. Figure 33b is enlarged view of the boxed area in Figure 33a. It shows that upon releasing the stored strain energy, not only joint segments fail in Mode I (blue) and Mode II (pink), but also rock mass fails in Mode I (black) and Mode II (red) adjacent to the deformation zone.

The figure also shows the particle velocity field by the orange arrows. It shows that upon earthquake activation, particle moving velocities at the foot wall and the hanging wall are opposite and larger velocities are concentrated at the core zone of the deformation zone. The velocities are decreasing with increasing distance from the core zone.

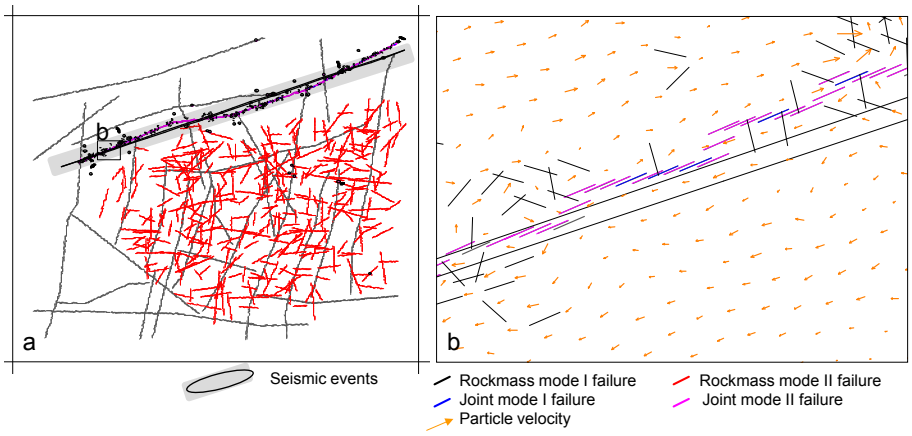

Figure 33. (a) View of the PFC model right after activation of earthquake at deformation zone ZFMWNW0809A showing failures of the bonds (in black the rock mass in failure Mode I, in red the rock mass in failure Mode II, in blue the joints in failure Mode I, in pink the joints in failure Mode II); (b) Detailed view of the box in (a) showing bond failures and particle velocity (orange arrows) in the rock mass, and failure mode of the smooth joints.

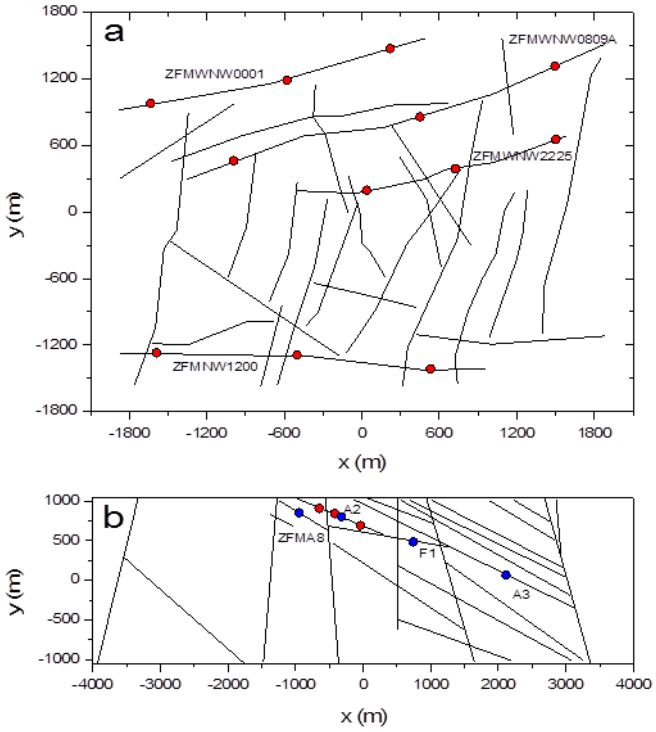

Figure 34. Distribution of seismometer particles along the earthquake hosting deformation zones for monitoring of peak slip velocity of an active earthquake in (a) horizontal (3 red seismometer particles placed at each zone) and (b) vertical section models (3 red seismometer particles placed along A2, and 4 blue seismometer particles placed at each zone for multiple zone earthquake modelling).

In order to record the peak slip velocity of the deformation zone by earthquake activation, three particles right adjacent to the core of the deformation zone are

assigned as seismometers to keep track of the slip velocity. Figure 34 shows the locations of the seismometer particles which are represented by black dots that are placed along the earthquake deformation zones, ZFMWNW0809A, ZFMWMW0001, ZFMWNW2225, ZFMNW1200. Figure 35 is an example of the earthquake modelling case, which shows changes in velocity of the seismometer particles along a deformation zone after activation of an earthquake. From such figures, only the peak velocity values from each curve are recorded. Only three seismometer particles are placed along the earthquake hosting deformation zone and recorded only the peak velocity. This is due to the fact that it requires large number of variables and much memory space to have many seismometer particles, and to monitor their velocities.

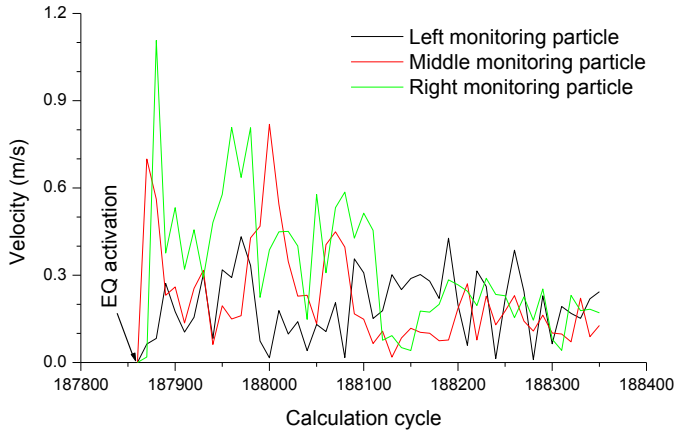

Figure 35. An example showing the changes of slip velocity at the seismometer particles along zone ZFMNW1200 activated under the glacially induced stress field at the time of maximum thickness of ice cover.

4.9. Modelling cases

Table 9 lists the 38 modelling cases covered in this study of which the results are discussed in Chapters 5 to 7. Descriptions on the key variations are provided at footnote of the table.

Table 9. Modelling cases performed in this study.

Loading condition[1] & model type (H/V[2])		Key variations of loading (Heating[3], Generic EQ DZ, Stress conditions[4], DFN[5])	Section in the report
T (H)	Operation (<1000 yrs)	Sim; mls; DFN03h	5.1
		Sim; mls; DFN06h	5.1
		Seq; mls; DFN03h	5.2
		Seq; mls; DFN06h	5.2
EQ (H)	Present Day	EQ@ZFMWNW0809A[6]; mls; DFN03h	6.1.1
		EQ@ZFMWNW0809A; mls; DFN06h	6.1.1
		EQ@ZFMWNW0001[7]; mls; DFN03h; dEQ[8]	6.1.2
		EQ@ZFMWNW0001; mls; DFN06h; dEQ	6.1.2
		EQ@ZFMWNW2225[9]; mls; DFN03h	6.1.3
		EQ@ZFMWNW2225; mls; DFN06h	6.1.3
	Forebulge	EQ@ZFMWNW0809A; gis1; DFN03h	6.2.1
		EQ@ZFMWNW0809A; gis1; DFN06h	6.2.1
		EQ@ZFMWNW0001; gis1; DFN03h; dEQ	6.2.2
		EQ@ZFMWNW0001; gis1; DFN06h; dEQ	6.2.2
		EQ@ZFMWNW2225; gis1; DFN03h	6.2.3
		EQ@ZFMWNW2225; gis1; DFN06h	6.2.3
		EQ@ZFMNW1200[10]; gis1; DFN03h	6.2.4
		EQ@ZFMNW1200; gis1; DFN06h	6.2.4
	Maxi ice Cover	EQ@ZFMWNW0809A; gis2; DFN03h	6.3.1
		EQ@ZFMWNW0809A; gis2; DFN06h	6.3.1
		EQ@ZFMWNW2225; gis2; DFN03h	6.3.2
		EQ@ZFMWNW2225; gis2; DFN06h	6.3.2
		EQ@ZFMNW1200; gis2; DFN03h	6.3.3
		EQ@ZFMNW1200; gis2; DFN06h	6.3.3
EQ (V)	Present Day	EQ@A2[11]; rsf; DFN03v	6.4.1
		EQ@A2; rsf; DFN06v	6.4.1
		EQ@A2-A3-A8-F1[12]; rsf; DFN06v	6.4.2
		EQ@A2-A3-A8-F1; rsf; DFN06v; dEQ	6.4.2
	Max ice Cover	EQ@A2; gisf2; DFN06v	6.5.1
		EQ@A2-A3-A8-F1; gisf2; DFN06v	6.5.2
		EQ@A2-A3-A8-F1; gisf2; DFN06v; dEQ	6.5.2
	Ice Retreat	EQ@A2; gisf3; DFN06v	6.6.1
		EQ@A2-A3-A8-F1; gisf3; DFN03v	6.6.2
		EQ@A2-A3-A8-F1; gisf3; DFN06v	6.6.2
		EQ@A2-A3-A8-F1; gisf3; DFN03v; dEQ	6.6.2
		EQ@A2-A3-A8-F1; gisf3; DFN06v; dEQ	6.6.2
T+EQ (H)	Operation (<1000 yrs)	Seq; EQ@ZFMWNW0809A; 50y; mls; DFN03h	7.1
		Seq; EQ@ZFMWNW2225; 50y; mls; DFN03h	7.2

Table 9. Cont. Modelling cases performed in this study. Footnotes.

[1] Loading conditions
- ✓ T: Thermal induced;
- ✓ EQ: Earthquake induced;
- ✓ T+EQ: Thermal and earthquake induced

[2] Model types
- ✓ H: horizontal section model (Fig.11);
- ✓ V: vertical section model (Fig.16)

[3] Heating
- ✓ Sim: All panels are heated simultaneously;
- ✓ Seq: Panels are heated in sequence, A→B→C→D

[4] *In situ* stress fields
- ✓ mls: most likely stress (Martin, 2007);
- ✓ gis1: glacial induced stress at the time of forebulge (mls+Δgis1);
- ✓ gis2: glacial induced stress at the time of maximum thickness of ice cover (mls+Δgis2);
- ✓ rsf: reverse stress field;
- ✓ gisf2: glacial induced stress field at time of maximum thickness of ice cover (rsf+Δgisf2);
- ✓ gisf3: glacial induced stress field at time of ice cover retreat (rsf+Δgisf3)

[5] Discrete Fracture Network (DFN)
- ✓ DFN03h: the most conservative realization in horizontal section model (Fig.11a);
- ✓ DFN06h: the least conservative realization in horizontal section model (Fig.11b);
- ✓ DFN03v: the least conservative realization in vertical section model (Fig.16a);
- ✓ DFN06v: the most conservative realization in vertical section model (Fig.16b)

[6] The longest deformation zone in the local model area also estimated unstable by the *CFS* analysis.

[7] Singö fault (truncated)

[8] dEQ: Direct earthquake simulation where shear force on the smooth joints is increased by a force multiplication factor to power-up the rupture/slide shear force, hence resulting in larger shear displacement and larger activation magnitude.

[9] The deformation zone posing the highest risk as it cuts across the three repository panels.

[10] The deformation zone estimated the most unstable in the all glacial induced stress conditions.

[11] The deformation zone estimated as the most unstable in the reverse stress field by SKB (Fälth et al., 2010).

[12] This modelling case assumes that deformation zones ZFMA2, ZFMA8, ZFMA3, and F1 are activated together at the same time, as they are closely spaced and connected.

4.10. Descriptions of plots of results

This section provides descriptions of the plots of results that are presented in Chapters 5 to 7. Five types of plots are provided for each of the modelling cases, which are:

- Type 1 plot (Figure 36): Spatial distribution of the thermal/earthquake induced seismic events and shear displacement of smooth joints that constitute the target fractures and deformation zones. Induced seismic events are ordered according to their magnitudes beside the plots. For the generic earthquake modelling cases, the earthquake magnitude is given as number in the plots and not included in the magnitude scaling of the induced seismic events since these are calculated for a width of 1 m in the out-of-plane direction. The hypocentre of the simulated earthquake is marked by a pink star. Shear displacement of the target fractures and deformation zones are shown by the colour coding, which is in logarithmic scale. Displacements coloured in red are shear displacements in 0.1-1 m range. Those coloured in green are those in 1-10 microns range.

- Type 2 plot (Figure 37): Shear displacement of target fractures and the deformation zones induced by an earthquake, e.g. at zone ZFMWNW0809A, with respect to the trace length of the target fracture and in comparison with several selected regressions in the literatures: WC1994 (Wells & Coppersmith, 1994), Dip-Slip (DS), Strike-Slip (SS) and Stable Continental Regions (SCR) data from Leonard (2010). The shear displacement at the earthquake hosting deformation zone is marked by a black star. The red horizontal line indicates the canister damage threshold for shear displacement on target fractures of 50 mm.

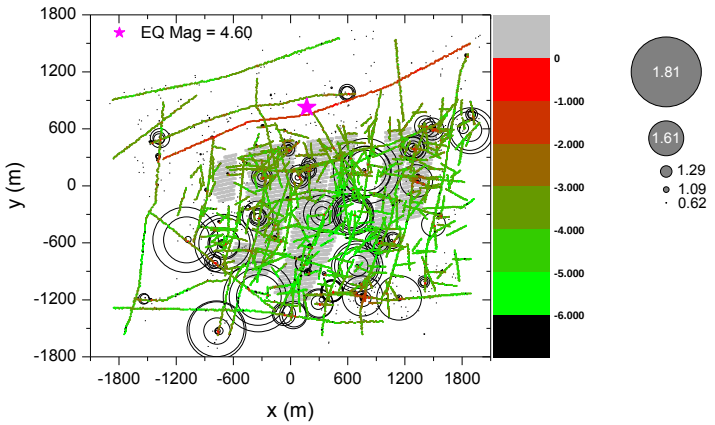

Figure 36. Spatial distribution of induced seismic events and shear displacements of smooth joints that constitute the target fractures and the deformation zones.

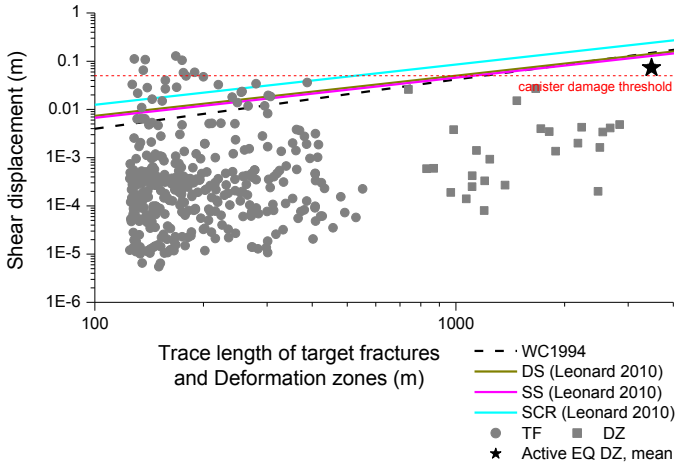

Figure 37. Relation of trace length of target fractures/deformation zones and their shear displacement.

- Type 3 plot (Figure 38): Box-and-whisker diagram of shear displacement of the target fractures divided into four trace length classes (class 1: 125-150 m, class 2: 150-200 m, class 3: 200-300 m, class 4: 300-600 m). This diagram is used to indicate whether a distribution is skewed and whether there are potential unusual observations (outliers) in the data set. Though it does not show a distribution in as much detail as a stem-and-leaf plot of an histogram do, the box-and-whisker plot is useful for comparing distributions because the median, mean, spread and overall range are evident. Descriptions of the elements in the box-and-whisker diagram are provided in Figure 39. Data points (observations) below the 5th percentile and above the 95th percentile are regarded as outliers in this report.

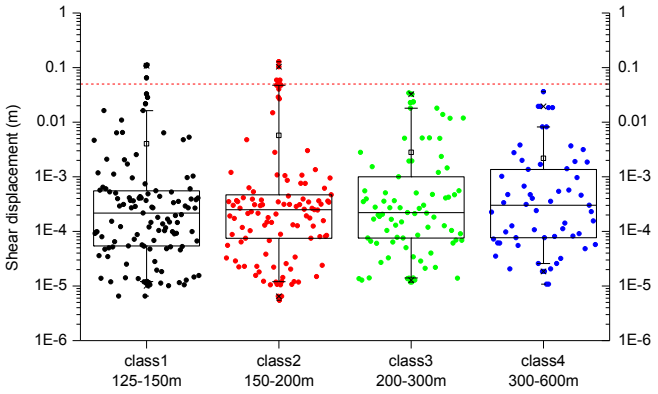

Figure 38. Box-and-whisker diagram of average shear displacement of the target fractures divided into four trace length classes.

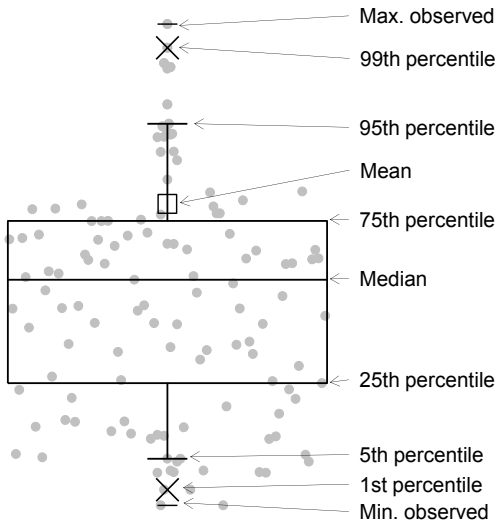

Figure 39. Description of the elements of the box-and-whisker diagram.

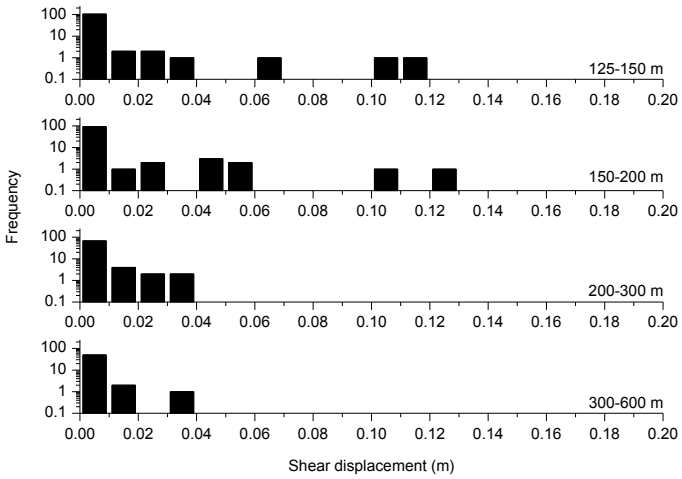

Figure 40. Histograms of the shear displacement of the target fractures divided into four trace length classes.

- Type 4 plot (Figure 40): Histograms of the shear displacement of the target fractures in four trace length classes (class1: 125-150 m, class2: 150-200 m, class3: 200-300 m, class4: 300-600 m). The vertical axes are in log scale for better readability of the frequencies.

- Type 5 plot (Figure 41): Box-and-whisker diagram of shear displacement of the smooth joints that contained in the target fractures in repository footprint (not the smooth joints contained in the deformation zones) in several classes of the distance from an active earthquake hypocentre to the smooth joints (class 1: 0-400 m, class 2: 400-600 m, class 3: 600-800 m, class 4: 800-1000 m, class 5: 1000-1200 m, class 6: 1200-1400 m, class 7: 1400-1600 m, class 8: 1600-1800 m, class 9: 1800-3000 m).

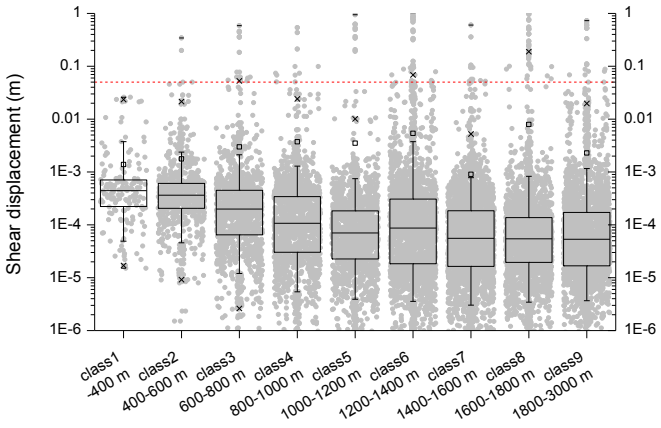

Figure 41. Box-and-whisker diagram of the shear displacement of smooth joints contained in the target fractures, divided into several classes of distance between the simulated earthquake hypocentre.

5. Modelling of thermally induced seismicity and target fracture responses

The modelling cases in this Chapter aim at investigating seismicity and responses of the target fractures due to the heating of the canisters disposed in all panels in the repository rock mass. The first part (Sec. 5.1) deals with simultaneous heat loading where it is assumed that all the canisters are disposed at the same time. The second part (Sec. 5.2) deals with sequential heat loading where it is assumed that the canisters are disposed in sequence, i.e. from panel A to panel D. Therefore, the start time of panel heating is different from panel to planel, and depends on the number of disposed canisters contained in the panels. Target fractures and deformation zones are shortened to "TFs" and "DZs".

5.1. Simultaneous heating

Figure 42 shows the thermally induced seismic events and shear displacement of the target fractures at 25 years after canister deposition for realization DFN03h, which is assumed to be the most conservative case of discrete fracture network. Multiple events with equivalent magnitude M1.64, 2.15, 2.27 and 2.16 (from left to right) occur at the same time and their midpoint is marked by the pink stars. The time at 25 years after deposition is chosen based on the observations in Min et al. (2014) where it was shown that the stresses at control points A to E in the repository give a maximum magnitude at 25 years after deposition (Figure 43).

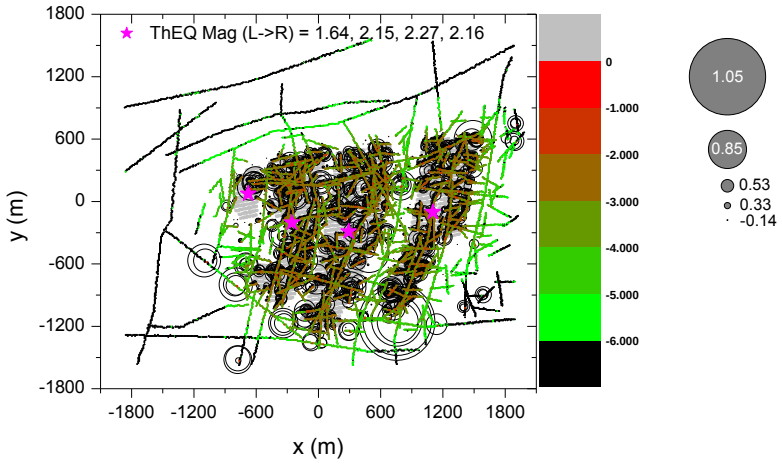

Figure 42. Spatial distribution of the induced seismic events and shear displacement of the smooth joints that constitute the TFs and DZs, due to 25 years of simultaneous heating with realization DFN03h (same as Figure A3-1).

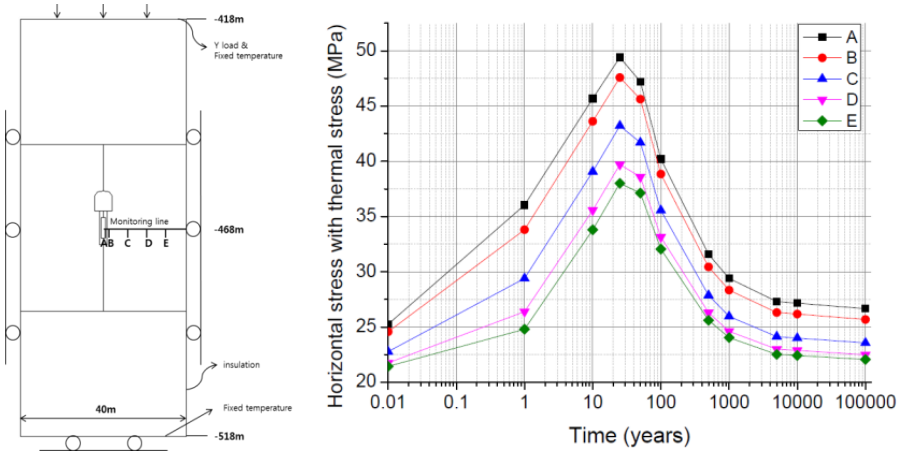

Figure 43. Model geometry for thermo-hydraulic modelling conducted in Min et al. (2014). Five monitoring points from A to E are placed on a horizontal line departing from the centre of the canister (Min et al., 2014). Evolution of horizontal components of thermal stresses at control points A through E at a depth of 468 m in Forsmark (Min et al., 2014).

Figure 42 shows that the TFs in the repository footprint are undergoing relatively larger shear displacement (in green) than those outside of the repository (in black). The four largest events are marked by stars and are induced by the heating of the panels. Thermally induced seismic events are concentrated within the footprint of the repository with magnitude mostly lower than M0.85. There are a few seismic events larger in magnitude, e.g. M1.05, outside the repository footprint and near the deformation zone intersection, i.e. between zone ZFMWNW0123 and zone ZFMENE0401A. The larger magnitude event occurs due to shear movement of zone ZFMENE0401A, which was under less critical state (see *CFS* in Figure 28), and is induced by the panel heating that triggers instability of zone ZFMWNW0123, which was judged to be unstable under the given stress condition. This result implies that even a DZ under stable state can slip due to the repository heating and such movement can lead to triggering of large shear displacement in limited parts of DZs that are in unstable state.

Figure 44 shows the relation between the trace length of the TFs and DZs and the shear displacements. It is observed that all the TFs are undergoing shear displacement lower than the canister damage threshold indicated by the red horizontal line (i.e. 50 mm). The length versus shear displacement data of TFs are investigated by the box-and-whisker diagram in Figure 45 showing that, shear displacement seems insensitive to trace length. Histograms of the shear displacement of TFs in Figure 46 also show shear displacements are below the canister damage threshold of 50 mm in all cases.

Results of modelling case with realization DFN06h, the least conservative case of discrete fracture network realization, are presented in Appendix 3 (Figure A3-5 to A3-8). The results are similar to those of realization DFN03h and show that all TFs are undergoing shear displacement lower than the canister damage threshold.

The results indicate no risk of canister damage is expected by the shear displacement of TFs exceeding 50 mm due to the thermal loading by the canisters of spent nuclear fuel disposed simultaneously.

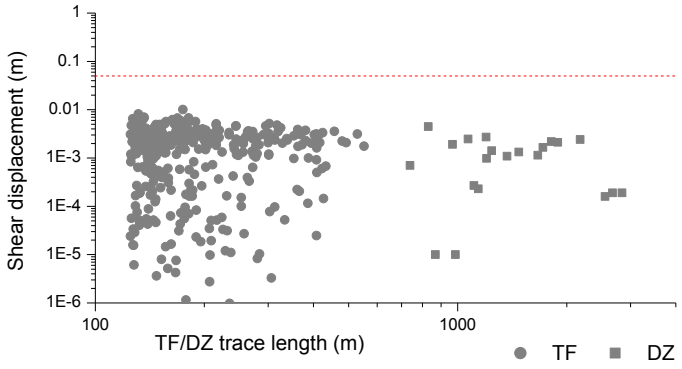

Figure 44. Shear displacement of the TFs and DZs with respect to length, due to 25 years of simultaneous heating with realization DFN03h (Fig.A-2).

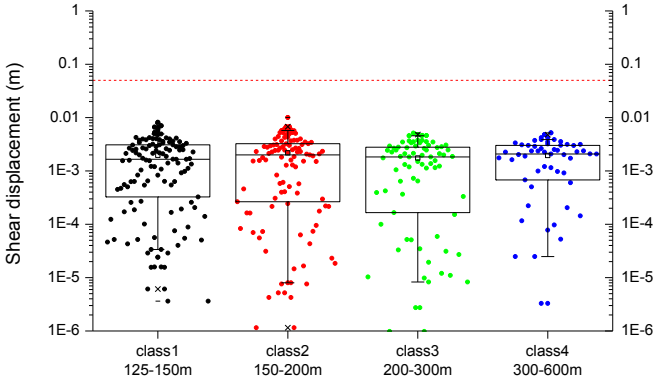

Figure 45. Box-and-whisker diagram of the shear displacement of TFs for four trace length classes, due to 25 years of simultaneous heating with realization DFN03h (same as Figure A3-3).

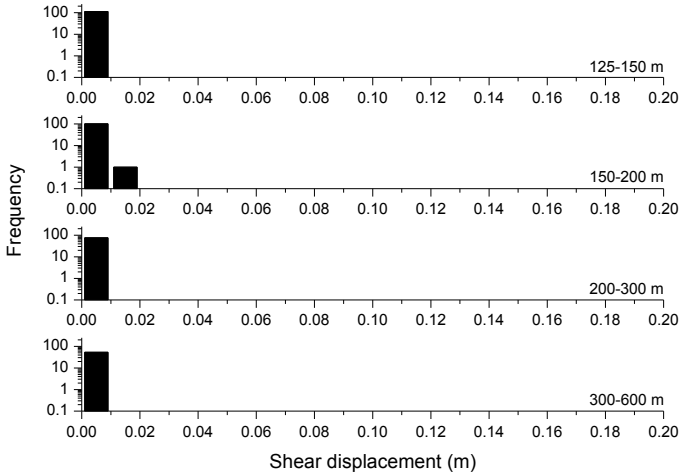

Figure 46. Histogram of shear displacement of the TFs in four different trace length classes, due to 25 years after simultaneous heating with realization DFN03h (same as Figure A3-4).

5.2. Sequential heating

This modelling case aims at investigating seismic events and responses of the target fractures due to heating of the repository rock mass by the canisters emplaced in sequential order panel by panel, i.e. from panel A to panel D.

Figure 47 shows the thermally induced seismic events and shear displacement of the TFs, 50 years after start of canister deposition in case of realization DFN03h, which is the most conservative case of discrete fracture network. Similarly to Figure 42, the figure shows that the TFs within the repository footprint are undergoing relatively larger shear displacement (in green) than those outside of the repository (in black). Star symbols indicate the hypocentres of the four largest seismic events generated by the sequential heating of each panel. It is observed that the more the canisters emplaced in a panel, the larger the magnitude of the events caused by their heating. Thermally induced seismic events are concentrated within the footprint of the repository and have magnitude mostly lower than M2.26. One magnitude M1.25 event is observed at the intersection of zone ZFMWNW0123 and zone ZFMENE0401A.

Figure 48 shows relation between the trace length of the TFs and DZs and shear displacements. It is observed that all the TFs are undergoing shear displacement lower than the canister damage threshold indicated by the red line (e.g. 50 mm). The length versus shear displacement data of TFs are investigated by the box-and-whisker diagram in Figure 49 showing that, taking into account a 95th percentile for defining a limit for outliers, reliable TFs shear displacement are even below 10 mm. This plot also shows no influence of the trace length on the shear displacement. The medians of the shear displacement of TFs are showing a slight increase for the shorter fractures. Histogram of the shear displacement of TFs in Figure 50 also shows that TFs are undergoing shear displacement below the canister damage threshold.

Results of modelling case with realization DFN06h, the least conservative case of discrete fracture network realization, are presented in Appendix 3 (Figure A3-13 to A3-16). The results are similar to those of realization DFN03h and show that all TFs are undergoing shear displacement lower than the canister damage threshold.

The results also indicate that no risk of canister damage is expected (i.e. shear displacement of TFs exceeding 50 mm) due to the thermal loading by the canisters of spent nuclear fuel disposed in sequential way.

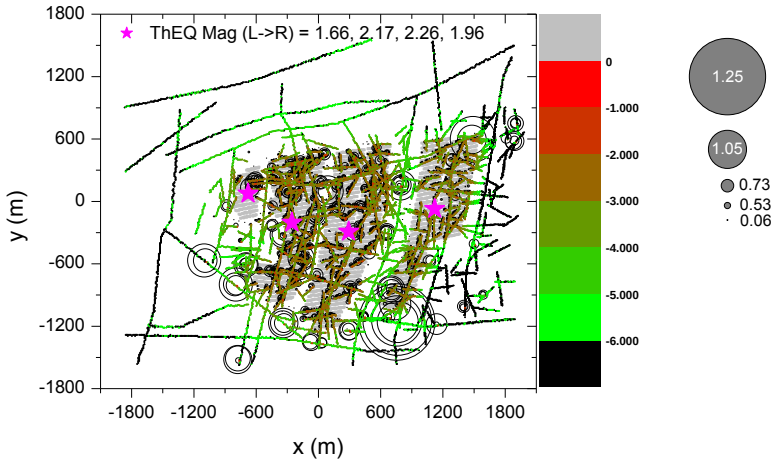

Figure 47. Spatial distribution of the induced seismic events and shear displacement of the smooth joints that constitute the TFs and DZs, due to 50 years of sequential heating with realization DFN03h (Fig.A3-9).

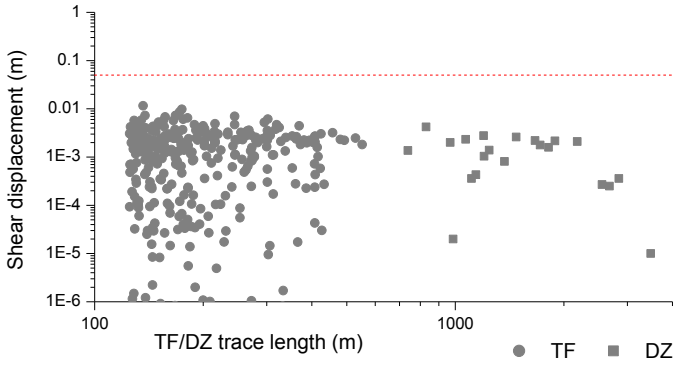

Figure 48. Shear displacement of the TFs and DZs with respect to length, due to 50 years of sequential heating with realization DFN03h (Fig.A3-10).

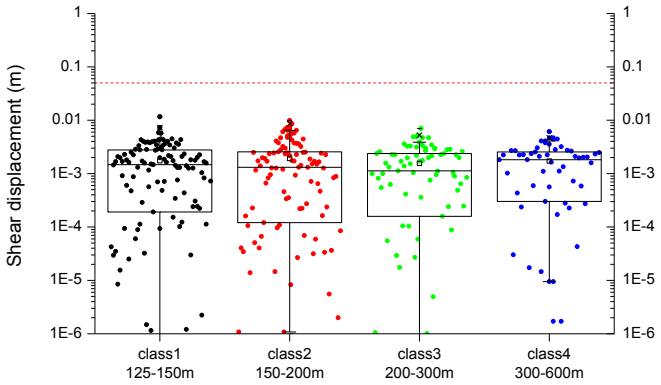

Figure 49. Box-and-whisker diagram of the TF shear displacement in four trace length classes, due to 50 years of sequential heating with realization DFN03h (Fig.A3-11).

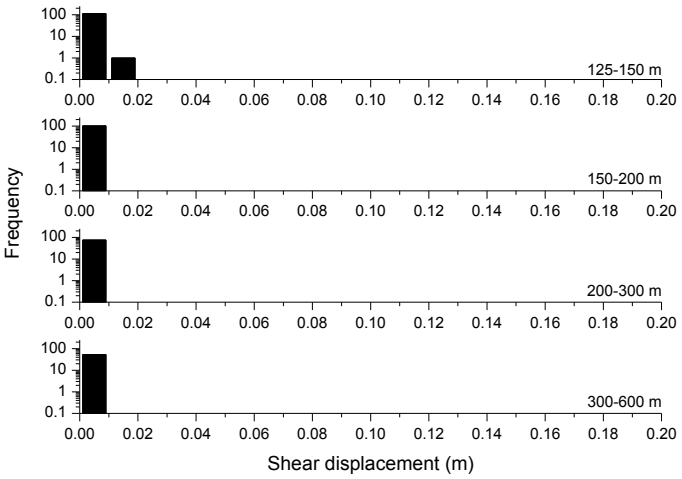

Figure 50. Histogram of shear displacement of the TFs in four different trace length classes, due to 50 years of sequential heating with realization DFN03h (Fig.A3-12).

5.3. The Consultants' assessment

Before starting to study the induced seismicity, validation of the thermal evolution of the repository is necessary. This is done by reproducing the temperature distribution in SKB's results in Hökmark et al. (2010). Figure 51 shows the contour plot of the rock temperature increase at repository level (460 m) at Forsmark resulting from simultaneous deposition modelled (a) in Hökmark et al. (2010) and (b) in this study with PFC. The selected time point is 50 years after completion of simultaneous deposition. The comparison of the two figures shows that the increase of rock temperature at the perimeter of the repository footprint is similar (in green to light blue). However, the temperature distribution within the repository footprint shows higher values in Hökmark et al. (2010) than in the PFC modelling. This is due to difference of the modelling approaches, i.e. the FEM method in SKB's study versus DEM method in PFC. In the PFC modelling, the temperature increase results in thermal stress that might lead to bond failure at some particle contacts. Such bond failure work as a barrier that hinders thermal conduction that occurs through the particle contacts, and this leads to very localized concentration of high rock temperature as shown in Figure 51b. However, as can be seen when comparing with Figure 51a, the temperature distribution in the PFC model is rather uniform, i.e. mostly yellow to orange colours, within the repository footprint. This is due to the modelling option chosen in the PFC thermal modelling, where the heat conduction is allowed as long as the particles are making contacts, even by the re-contacts after bond breakages. However, heat conduction is not allowed if particles are separated.

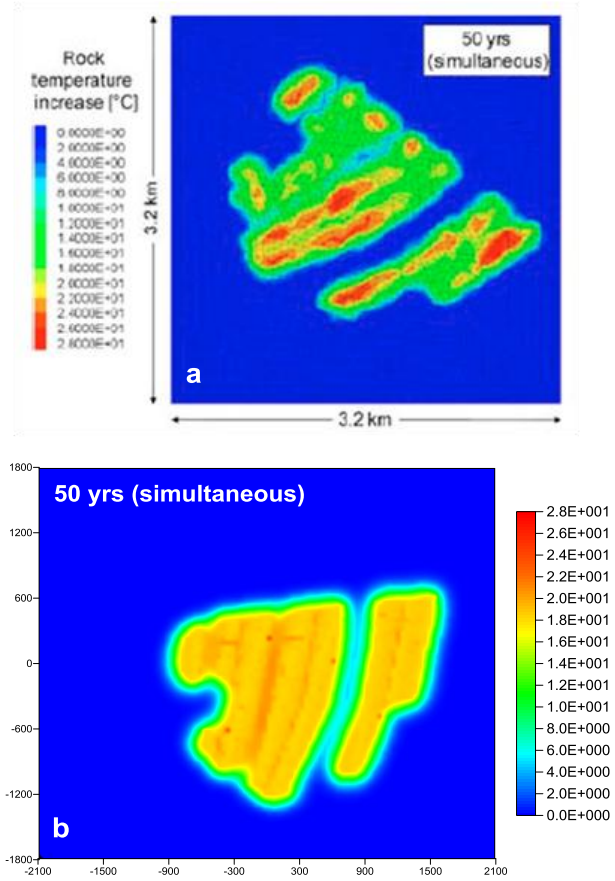

Figure 51. Contour plots of the rock temperature increase at repository level (460 m) at Forsmark modelled in (a) Hökmark et al. (2010) and (b) in this study by PFC, at 50 years after simultaneous heating.

As a result of the thermal loading due to the decaying fuel, the rock mass expands and subsequently contract, which leads to changes in the stress field. These changes are monitored in both modelling cases where the repository panels are heated at the same time and in sequential order. Table 10 and 11 list the regional principal stresses that are monitored locally in different locations in the model. The numbering of the local stress monitoring areas is the same as in Figure 22. For each monitoring area, the initial major and minor principal stresses are monitored in the measurement areas. The principal stresses are also monitored at certain times after the start of heating. The last column indicates the relative difference between the initial stresses and the stresses after heating.

The initial principal stresses before applying the heat are close to 40 MPa and 22 MPa, which are far-field major and minor principal stresses, respectively, in the "most likely" stress field by SKB. Slight deviations are observed due to local effect that depends, for example, on the regional density of the pre-existing fractures and their irreversible slip. Among the five monitoring areas, Area 1 shows the largest difference between the stress before and after heating. This is due to the fact that the Area 1 is located within the repository footprint. Area 2 and 5 are located outside the footprint of the repository and the stress state in these areas is less influenced by the heating.

Decrements in the stresses in some monitoring areas are due to failure of the rock mass and target fractures due to the heating. However, Area 3 in Table 11 shows increments both in major and minor principal stresses. This is due to the fact that at time of 50 years after start of heating the in panel A, heating of the panel D has just started. Therefore, the rock mass starts to expand and this leads to stress increases. However, the difference is expected to decrease below zero as heating would induce failures of rock mass and failure/slip of the target fractures. Regardless of the time or the order of panel heating, stresses in Area 5 show increase due to the heat induced expansion of the repository rock mass.

Table 10. Local principal stresses measured at different locations within the repository footprint before and after 25 years of simultaneous heating and their difference.

Area	Initial (MPa)		After heating (MPa)		Increment (MPa)	
no.[+]	σ_1	σ_2	σ_1	σ_2	$\Delta\sigma_1$	$\Delta\sigma_2$
1	38.3	22.1	35.4	21.5	-2.9	-0.6
2	38.7	21.7	38.4	21.9	-0.3	+0.2
3	37.9	21.5	37.2	22.3	-0.7	+0.8
4	37.3	21.8	36.4	22.3	-0.9	+0.5
5	37.4	21.9	37.6	22.0	+0.2	+0.1

[+] Area numbers correspond to the local stress monitoring circles shown in Figure 22.

Table 11. Local principal stresses measured at different locations within the repository footprint before and after 50 years of sequential heating and their difference. See footnotes in Table 10.

Area	Initial (MPa)		After heating (MPa)		Increment (MPa)	
no.[+]	σ_1	σ_2	σ_1	σ_2	$\Delta\sigma_1$	$\Delta\sigma_2$
1	38.3	22.1	35.4	21.6	-2.9	-0.5
2	38.7	21.7	38.3	21.9	-0.4	+0.2
3	37.9	21.5	38.3	21.8	+0.4	+0.3
4	37.3	21.8	36.6	22.2	-0.7	+0.4
5	37.4	21.9	37.6	22.0	+0.2	+0.1

[+] Area numbers correspond to the local stress monitoring circles shown in Figure 22.